Oh, J., Lee, I., Stuart, F. M., Park, M. and Kim, J. (2021) EM1-signature in the North Fiji Basin: evidence for stagnant slab-derived mantle upwelling beneath the trench-distal back-arc basin. *Journal of Geophysical Research: Solid Earth*, 126(4), e2020JB021017.

(doi: 10.1029/2020JB021017)

This is the peer reviewed version of the following article:

Oh, J., Lee, I., Stuart, F. M., Park, M. and Kim, J. (2021) EM1-signature in the North Fiji Basin: evidence for stagnant slab-derived mantle upwelling beneath the trench-distal back-arc basin. *Journal of Geophysical Research: Solid Earth*, 126(4), e2020JB021017, which has been published in final form at: 10.1029/2020JB021017

https://eprints.gla.ac.uk/236546/

Deposited on: 16 March 2021

EM1-signature in the North Fiji Basin: Evidence for stagnant slab-derived mantle upwelling beneath the trench-distal back-arc basin

Jihye Oh[1, 2], Insung Lee[2], Finlay M. Stuart[3], Munjae Park[2, 4] and Jonguk Kim[1*]

[1]Deep-sea and Seabed Mineral Resources Research Center, Korea Institute of Ocean Science & Technology, Busan, Republic of Korea

[2]School of Earth and Environmental Sciences, Seoul National University, Seoul, Republic of Korea

[3]Isotope Geoscience Unit, Scottish Universities Environmental Research Center, East Kilbride, UK

[4]Department of Earth and Environmental Sciences, Chungbuk National University, Cheongju, Republic of Korea

*Corresponding author: Jonguk Kim (jukim@kiost.ac.kr)

Key Points:

- New geochemical data of the basalts from the North Fiji Basin reveal a signature of enriched mantle 1 (EM1) near the Fiji Triple Junction

- The enriched basalts contain both primordial helium inherited from mantle transition zone and dehydrated oceanic slab component

- Upwelling of hydrous mantle transition zone triggered by stagnant slab can be the source of enriched mantle in mature back-arc basins

Abstract

Basaltic volcanism at the mature back-arc spreading axis in the North Fiji Basin (NFB) exhibits significant geochemical heterogeneity from depleted mid-ocean ridge basalt (MORB) to enriched MORB compositions. The volatile and Sr–Nd–Pb–He isotope composition of basaltic glasses from the Central Spreading Ridge (CSR) of the NFB suggests that a second enrichment mantle component is present in addition to the previously observed Samoan mantle plume. The hydrous OIB-like basalts from the northern CSR have a weak enriched mantle 1 (EM1) isotopic signature and negative correlation between Ba/Th and Zr/Hf ratios, similar to rejuvenated Samoan lavas associated with tectonic driven volcanism. The EM1 signature is distinct from shield-stage Samoan basalts and back-arc basin basalts from the Lau Basin by high Ba/La ratio and negative correlation between Ba/Th and Ba/Ta ratios, indicating contributions from dehydrated and altered oceanic crust and sediments. Our new geochemical data suggest that focused melting above the mantle transition zone (MTZ) triggered by dehydration of stagnant slab can be a source of the EM1-like melts containing both elevated ^{3}He/^{4}He ratios (up to 12.52 R_A) and altered oceanic slab components. Given the spatial coincidence of the inferred EM1 basalts with the clustered deep earthquakes, our results support the presence of detached oceanic slabs in the mantle transition zone beneath the northern NFB.

Plain Language Summary

This work provides interpretation of mantle enrichment process occurred in mature and plume-distal oceanic back-arc basins. Providing geochemical data set of basaltic glasses collected from the central spreading ridge in the North Fiji Basin indicates mantle heterogeneity, which can be explained by mixing between the depleted ambient mantle and the enriched mantle reservoir present in the shallow mantle depth. The enriched basalts contain both primordial helium contributed from mantle transition zone and dehydrated oceanic slab component. They are emplaced above deep earthquake clusters indicating slab stagnation in depths of the mantle transition zone. Thus, we suggest focused hydrous mantle upwelling at the edge of detached slabs lying in the mantle transition zone as the shallow origin for the enriched magmatism in plume-, trench-distal back-arc basins.

1 Introduction

Intraplate magmatism is generally attributed to mantle plumes that originate from the core–mantle boundary (i.e., the D'' layer at a depth of 2,900 km; Morgan, 1971). Upwelling mantle plumes are also an important source of geochemical heterogeneity in the upper mantle, which is reflected by the presence of geochemically and isotopically enriched magmas at mid-ocean ridges and subduction zones. Shallow hydrous mantle ascending from stagnant slabs in the mantle transition zone (MTZ) at depths of 410–660 km have been proposed to explain continental intraplate volcanism, for instance Cenozoic alkaline basalts in northeastern Asia (Kuritani et al., 2011; Kuritani et al., 2019; Wang et al., 2017; Yang & Faccenda, 2020). Yang & Faccenda (2020) presented a model for the generation of melts above the stagnant Pacific slab by hydration events of MTZ, which is considered to trigger the overlying intraplate volcanism distal from the active subduction zone, the Japan Trench. In this case, metasomatism of the MTZ by ancient slab stagnation has been invoked to explain the origins of enriched mantle 1 (EM1)-type geochemical signature in the basalts (Kuritani et al., 2011).

63   Although recent studies of shallow mantle plumes induced by a stagnant slab have
64 focused on continental areas, similar processes can occur in mature oceanic back-arc basin
65 systems above subducted slabs. Since the identification of the stagnant, subducted Pacific Plate
66 oceanic slab at a depth of 550 km beneath the Izu–Bonin region (Okino et al., 1989), additional
67 stagnant slabs have been identified in the southwestern Pacific (e.g., Tonga; Van der Hilst, 1995),
68 Calabria (Selvaggi & Chiarabba, 1995), and Scotia (Bijwaard et al., 1998). Despite the potential
69 for stagnant slabs to influence melt generation in back-arc basins (Faccenna et al., 2010), they
70 have attracted little attention.

71   The North Fiji Basin (NFB) is a mature back-arc basin located at the margin of the
72 southwest Pacific (Fig. 1), and provides an ideal opportunity to examine the influence of slab
73 stagnation on magmatism within the oceanic plate. Deep earthquakes occurring at depths of ~600
74 km beneath the NFB have been interpreted as evidence of detached, stagnant slabs in the MTZ
75 (Chen & Brudzinski, 2001; Martin, 2014; Okal & Kirby, 1998). Several geophysical studies have
76 suggested that mantle upwelling triggered by stagnant slabs, has induced magmatism in the
77 central part of the basin (Chen & Brudzinski, 2001; Faccenna et al., 2010; Richards et al., 2011).
78 Ocean island basalt (OIB)-like basalts in the northern segments of the Central Spreading Ridge
79 (CSR) have previously been attributed to the lateral flow of the Samoan mantle plume (A. Price
80 et al., 2014, 2017). However, ^{3}He/^{4}He ratios and carbon isotope data indicate that the source does
81 not have a significant deep mantle contribution (Nishio et al., 1998). In addition, the EM1-like
82 Sr–Nd isotope signature of the enriched NFB basalts is distinct from the Samoan mantle plume-
83 influenced volcanic rocks from the northern Lau Basin (Lytle et al., 2012), and thus requires
84 another enriched mantle source. Here we present new geochemical data, including H_2O and CO_2
85 contents, and Sr–Nd–Pb–He isotope data for basaltic glasses from the CSR in the NFB in order
86 to assess whether a shallow, hydrous plume from a stagnant slab was responsible for the
87 geochemical enrichment.

2 Geological setting and sampling

89   The NFB initially opened at 12 Ma in response to the subduction of the Australian Plate
90 at the New Hebrides Trench after a change in subduction polarity from the now inactive Vitiaz
91 Trench, due to the collision of the Ontong–Java Plateau (Auzende et al., 1988; Meffre &
92 Crawford, 2001; Schellart et al., 2006). According to the "double-saloon door" model describing
93 the tectonic evolution of the NFB (Martin, 2013), opposite rotations of the divided Vitiaz paleo-
94 arc, Vanuatu arcs, and Fiji Platform formed numerous segmented back-arc spreading ridges that
95 are both parallel and perpendicular to the present-day Vanuatu Arc (Fig. 1a).

96   The N–S-trending, arc-parallel spreading axis between 14.5º and 22ºS (i.e., the CSR) is a
97 major active spreading system in the central and southern NFB. It is divided into four main
98 segments with intermediate spreading rates (5–8 cm/yr) (Eissen et al., 1991, 1994) (Fig. 1b). The
99 northernmost segment (N160) is approximately 200 km in length and is an arm of a ridge–ridge–
100 fracture (R–R–F) zone-type triple junction at 16º50′S (i.e., the Fiji Triple Junction). The segment
101 comprises two symmetrical elevated ridges that are ~30 km wide, which increase in width
102 towards the Fiji Triple Junction (Lafoy et al., 1990). The Fiji Triple Junction has a complex
103 topography that has been caused by large-scale lithospheric stress (Nohara et al., 1994). High-
104 amplitude rises are present at the triple junction that do not occur along the southern segments,
105 indicating strain concentration at the triple junction (Auzende et al., 1988; Lafoy et al., 1990).
106 This reflects variable magma productivity associated with thermal variations in the upper mantle

107 (Zhang & Pysklywec, 2006). Zhang and Pysklywec (2006) suggested that hot, buoyant,
108 upwelling material in the upper mantle causes enhanced magma production and the anomalously
109 shallow seafloor in the central NFB. Ridge segment N15 is the southern arm of the triple
110 junction, is 120 km long, and has a spreading rate of 5–6 cm/yr. Segment NS is located between
111 18°10′ and 21°S, is 310 km in length, and has a morphology that is comparable to a typical mid-
112 ocean ridge system. The southernmost segment (174E; 120 km in length) is offset by ~90 km to
113 the east at the southern tip of the NS segment by an E–W-trending transform fault. The
114 southernmost segment links to the New Hebrides trench, which is the present-day subduction
115 zone.

116 The Hazel Holmes Ridge, South Pandora Ridge, and Tripartite Ridge are arc-
117 perpendicular ridge segments located in the northern NFB (Fig. 1a; Garel et al., 2005). The
118 Cikobia Spreading Center and Futuna Spreading Center are located in the eastern Tripartite
119 Ridge and trend 30ºE and 60ºE, respectively. Despite the ultra-slow and slow spreading rates
120 (1.6–4.0 cm/yr) of these spreading centers, their segmented ridges exhibit contrasting axial
121 morphologies, indicating that intermittent volcanic activity has been induced by temporal–spatial
122 variations in upper mantle convection cells beneath this region (Garel et al., 2005; Pelletier et al.,
123 1998; R. Price & Kroenke, 1991).

124 During the expeditions of R/V Onnuri by Korea Institute of Ocean Science and
125 Technology (KIOST) in 2003 and 2012, basalt samples were dredged from 33 stations along the
126 volcanic ridges of the CSR (Fig. 1; see Table S1). The glassy chilled margins were separated
127 from the recovered rock samples and crushed into chips smaller than 1 mm using a jaw crusher.
128 Fresh glass chips were handpicked under a stereo microscope, reacted with 1 M HCl in an
129 ultrasonic bath for 10 min at room temperature, and rinsed three times with deionized water to
130 remove surface contaminants on the surfaces of the glass fragments.

3 Analytical methods

132 Major elements were analyzed with a Thermo Jarrell–Ash ENVIRO II inductively
133 coupled plasma emission spectrometer at Activation Laboratories, Canada. The powdered
134 glasses were mixed with lithium metaborate and lithium tetraborate, fused in an induction
135 furnace, and then digested in 5% nitric acid (Kim et al., 2017). The analyses were performed in
136 batches including a reagent blank and six certified reference materials from USGS (BIR-1, DNC-
137 1 and W-2), CCRMP (SY-4), IGGE (GWB07113) and NIST (NIST 694) (see Table S2).
138 Precision is 0.4–1.0% for SiO_2, Al_2O_3, K_2O, MnO, CaO, Na_2O and TiO_2, 1.2–1.5% for FeO_T,
139 MgO and 3.8% for P_2O_5. Measured reference materials were within 5% of preferred and certified
140 values, except low abundance elements (see Table S2). The major element contents of some
141 glass chip samples were analyzed using a Shimadzu Electron Probe Microanalyzer (EPMA-1600)
142 at Korea Basic Science Institute (KBSI) in Jeonju center, South Korea. Operating conditions
143 were 15 kV accelerating voltage, 20 nA beam current, and 10 µm beam diameter for spot
144 analyses. Natural and synthetic minerals were used as standards and the ZAF correction method
145 was used for data reduction. The EPMA analyses have a precision of 1.1–5.0% for most of major
146 elements, except for P_2O_5 (7.1%) and MnO (11.6%). Basaltic glass standard of USGS (BCR-2G)
147 was run as unknown sample and the measured data for major elements were within 4.4% of
148 preferred values, except MnO (10%) (Table S2).

149 Volatile abundances (H_2O and CO_2) were measured using a Nicolet 6700 Fourier
150 transform infrared (FTIR) spectrometer and Continuum microscope in the School of Earth and

151 Environmental Sciences, Seoul National University, Seoul, South Korea. Doubly polished glass
152 wafers (110 μm thick) were analyzed. A 100 × 100 μm IR beam was transmitted through clear
153 sites on 2–5 separate wafers for each sample in a chamber purged with N_2, in order to remove the
154 interference from atmospheric water and carbon dioxide. The peaks of the absorbance band at
155 3540 cm^{-1} for H_2O and 1515–1435 cm^{-1} for CO_2 were measured with OMNIC software, and the
156 total dissolved H_2O and CO_2 contents were calculated using the Beer–Lambert law with
157 absorption coefficient (ε), 63 and 375 mol^{-1}cm^{-1}, respectively (Dixon et al., 1988; Kelley et al.,
158 2006; Stolper, 1982), with a reproducibility of $< \pm 5\%$.

159 After FTIR analysis, the glass wafers were mounted in epoxy resin and re-used for trace
160 element analysis by laser ablation ICP–MS, using an Agilent 7700X coupled to a New Wave
161 Research 193 nm laser at KIOST. The sample surface was ablated for 40 s after 60 s of
162 background measurement. The laser was focused to a 105 μm beam diameter, with a 2 J/cm^2
163 fluence and 5 Hz repetition rate. The analyses were performed with ThO$^+$/Th$^+$ < 0.4%, 1350 W
164 RF power, 1.4 V RF matching, and 0.02 s dwell times for each element. In a single analytical run,
165 every seven sample analyses were bracketed by a NIST 612 analysis (primary reference material
166 for external calibration) and BCR-2G (data quality control). To correct for the matrix effect
167 between the primary reference material and samples, internal standardization was conducted
168 using the ^{43}Ca concentration. The acquired data were processed using Iolite v3.32 software
169 (http://iolite-software.com) and seven different ablations were averaged for each sample. The
170 analytical precision for trace elements is 3.4–9.8%, except Be (17%). The measured trace
171 element concentrations of BCR-2G (n=25) were within 10% of preferred values, except for Be
172 (13%), Ni (22%), Cu (11%), and Zn (38%) (see Table S2).

173 A Thermo Fisher TRITON Plus thermal ionization mass spectrometer (TIMS) and a
174 Thermo Fisher Neptune multi-collector inductively coupled plasma mass spectrometer (MC–
175 ICP–MS) housed at the National Oceanography Centre Southampton (NOCS) were used to
176 acquire Sr, Nd, and Pb isotope data, respectively. For Sr and Nd, volcanic glasses were digested
177 with HF/HNO$_3$ on a hotplate in sealed Savillex vials, the Sr is isolated using an approximately 70
178 μL column of Sr-Spec resin with 3M HNO$_3$ to remove interfering elements, followed by
179 collection of the Sr in water. The purified samples were loaded onto an outgassed Ta filament
180 prior to analysis on a TIMS. The Sr isotope measurements were carried out with a multidynamic
181 peak jumping routine at a constant beam intensity of 2 V and were adjusted for mass
182 fractionation using a linear-law based on the average value obtained for NBS987 standard
183 (^{87}Sr/^{86}Sr of 0.710248 ±0. 23 (2σ)).

184 Solutions for Nd using the same digest as for Sr were subsampled to give approximately
185 200ng of Nd. The Nd purified using a two-column procedure. First a 200 μL cation exchange
186 column to remove the major elements followed by an approximately 300 μL Ln-Spec column to
187 isolate the Nd. The samples were then analyzed on a MC-ICP-MS following the Lang et al.
188 (2014). Mass bias corrected ratios were normalized to the given ^{143}Nd/^{144}Nd value (0.512115) of
189 the standard JNdi-1 (Tanaka et al., 2000). Measured values for the JNdi standard were
190 ^{143}Nd/^{144}Nd = 0.512116 ± 6 (2σ)).

191 Sample processing and analysis of Pb isotopes closely followed Taylor et al. (2015).
192 Glass samples were dissolved in ~4 ml of HF/HNO$_3$ mixture. Pb was purified with a two-stage
193 anion exchange resin-filled column procedure using HBr and HCl. The amount of Pb in
194 procedural blanks was generally <75 pg. The samples were analyzed using a double spike

195 technique to correct for fractionation and mass bias. The 2σ uncertainties on standard NBS 981
196 ($^{206}Pb/^{204}Pb$ = 16.9409, $^{207}Pb/^{204}Pb$ = 15.4974, and $^{208}Pb/^{204}Pb$ = 36.7145) were 0.0034, 0.0028,
197 and 0.0073 for $^{206}Pb/^{204}Pb$, $^{207}Pb/^{204}Pb$, and $^{208}Pb/^{204}Pb$, respectively.

198   Helium isotopic compositions were analyzed with a Thermo Fisher HELIX-SFT mass
199 spectrometer at the Scottish Universities Environmental Research Centre (SUERC) (Carracedo et
200 al., 2019). Gases were extracted from the vesicles of ~1 g of glass chips by *in vacuo* crushing.
201 The He was purified using two hot GP50 Zr–Al alloy getters and liquid N-cooled charcoal
202 (Stuart et al., 2000). The reproducibility of the measurements was determined as $\pm0.5\%$ (1 SE)
203 using the certified value of an internal He standard (HESJ; $^{3}He/^{4}He$ = 20.63 R_A; Matsuda et al.,
204 2002).

4 Results

205

206   4.1. Major and trace elements

207   Concentrations of major and trace elements in the CSR glass samples are listed in Table
208 S1. All samples are subalkaline basalts with a narrow range of SiO_2 contents (48.9–51.9 wt.%)
209 (Fig. 2a). Systematic variations are evident in major element versus MgO diagrams (Fig. 2b–i).
210 Most samples with low alkali contents (< 3.5 wt.%) are distributed along the liquid line of
211 descent (LLD) for sample DGFB120901, with the lowest SiO_2 (48.9 wt.%) and alkali contents
212 (1.87 wt.%) of the CSR samples, at assumed initial conditions of 0.06 wt.% H_2O and 0.1 kbar.
213 However, several samples from the northern CSR (N160, Fiji Triple Junction, and N15), with
214 higher alkali contents (> 3.5 wt.%), exhibit another trend with lower FeO and CaO and higher
215 K_2O contents at a given MgO content. This trend is broadly consistent with the LLD for sample
216 DGFB121403 with the highest MgO content (7.79 wt.% MgO) of the high alkali content samples
217 (Fig. 2b–i), at an assumed initial water content and pressure of 1 wt.% H_2O and 2 kbar,
218 respectively.

219   Primitive mantle-normalized incompatible trace element and chondrite-normalized rare
220 earth element (REE) patterns are shown in Fig. 3. The CSR basalts vary from extremely depleted
221 MORB- to OIB-like compositions with $(La/Sm)_N$ = 0.31–3.07 and variable degrees of light REE
222 (LREE) enrichment relative to heavy REEs (HREEs; $(La/Yb)_N$ = 0.26–8.13). The samples with
223 E-MORB and OIB chemistry are relatively depleted in highly incompatible, large-ion lithophile
224 elements (LILEs; i.e., Rb, Ba, Th, and U) compared to high-field-strength elements (HFSEs; e.g.,
225 Nb and Ta). The depleted N-MORB-like samples show no significant depletion in HFSEs.
226 Negative anomalies for fluid-mobile elements (e.g., Pb and Sr) and Ti (Fig. 3a) suggest that there
227 is no significant subduction component in the back-arc basin mantle. The OIB-like basalts have
228 high alkali content and $(La/Sm)_N$ > 2, which is higher than the general criteria used for
229 discriminating E-MORBs ($(La/Sm)_N$ > 1 from Arevalo & McDonough, 2010; $(La/Sm)_N$ > 1.5
230 from Gale et al., 2013) (Fig. 2). The relatively depleted samples ($(La/Sm)_N$ < 2) have major
231 element compositions defined by the fractionation trend for sample DGFB120901 (Fig. 2). Based
232 on geochemistry, the CSR basalts can be divided into two groups, the enriched OIB-like basalts
233 ($(La/Sm)_N \geq 2$) and relatively depleted MORB-like basalts ($(La/Sm)_N$ < 2), as represented by
234 samples DGFB121403 and DGFB120901, respectively.

235   4.2. H_2O and CO_2

236   Water and CO_2 contents of the glasses are listed in Table S1 (0.06–1.22 wt.% H_2O; 23–
237 332 ppm CO_2). Based on the saturation curve for basaltic melts (Byers et al., 1983), the H_2O

238   contents of the CSR glasses are below the saturation level (Fig. 4a), but some CO_2 contents are
239   above the saturation level for the sampling depths, which indicates that CO_2 is over-saturated
240   (Fig. 4b). More specifically, most samples from the NS segment are CO_2 supersaturated (116–
241   332 ppm) despite a relatively narrow range of H_2O (0.06–0.29 wt.%; Fig. 4b–c). This is a
242   common feature of MORB where CO_2-rich magma ascends rapidly and there is insufficient time
243   for degassing (Dixon et al., 1988; Dixon & Stolper, 1995). Except the CO_2-supersaturated
244   samples, most CSR glasses plot beneath the vapour-saturated curve of 400 bar (Fig. 4c) and their
245   calculated equilibrium depths exhibit a positive correlation with sampling depth (Fig. 4d).

246   The H_2O contents of the CSR basalts also vary significantly with $(La/Sm)_N$ ratios (Fig.
247   4a). The samples with enriched compositions ($(La/Sm)_N \geq 2$) have higher H_2O contents (> 0.63
248   wt.%) relative to CO_2 (23–107 ppm), compared with the depleted samples (0.06–1.13 wt.% H_2O;
249   24–332 ppm CO_2). The volatile contents of the enriched samples are in the range of those for
250   Samoan OIBs, whereas those of the depleted samples (including the CO_2-supersaturated samples)
251   are comparable to MORBs (Fig. 4c).

252   4.3. Sr–Nd–Pb–He isotopes

253   Isotope data for the CSR basalts are listed in Table S1. Sr–Nd–Pb isotope ratios ($^{87}Sr/^{86}Sr$
254   = 0.702809–0.703727, $^{143}Nd/^{144}Nd$ = 0.512825–0.513178, and $^{206}Pb/^{204}Pb$ = 17.5697–18.6702)
255   cover the range from extremely depleted to enriched MORB compositions, and are consistent
256   with previous studies (Aggrey et al., 1988; Eissen et al., 1991, 1994; Nohara et al., 1994; A.
257   Price et al., 2014, 2016; R. Price et al., 1990; R. Price & Kroenke, 1991). The heterogeneous
258   isotopic compositions require mixing of multiple mantle sources, as is also evident from the
259   major, trace, and volatile element data. Co-variations of isotope data and $(La/Sm)_N$ ratios
260   confirm the bimodal grouping identified from trace element geochemistry. The enriched basalts
261   from northern CSR have radiogenic Sr–Pb and less radiogenic Nd compared with the other
262   samples that are similar to depleted MORB mantle (DMM; Nohara et al., 1994; Workman &
263   Hart, 2005) (Fig. 5).

264   The CSR samples define a linear array that extends toward the EM1 component in Sr–Nd
265   isotope space, which deviates from the mantle mixing line proposed for volcanic rocks from
266   back-arc spreading centers in the northern Lau Basin (Nebel & Arculus, 2015; Fig. 5a). Although
267   the depleted samples from the CSR and northern Lau Basin plot within the field for DMM, the
268   enriched CSR samples have the EM1-like feature of significantly lower $^{87}Sr/^{86}Sr$ at a given
269    $^{143}Nd/^{144}Nd$ compared with the most enriched northern Lau Basin samples.

270   With the exception of one sample from the Fiji Triple Junction, helium isotopic
271   compositions have a narrow range (8.2–9.7 R_A; see Table S1) that is consistent with previously
272   reported data from the CSR (7.9–10.3 R_A; Marty & Zimmermann, 1999; Nishio et al., 1998;
273   Price et al., 2014). $^3He/^4He$ ratios are on average (9 ± 0.4 R_A) slightly higher than typical DMM
274   (8 ± 1 R_A; Graham, 2002; Kurz et al., 1982). The elevated $^3He/^4He$ ratios do not appear to be
275   dependent on the absolute content of ^4He (Fig. 6a). For the depleted CSR group ($(La/Sm)_N < 2$),
276   there is weak negative correlation between $^3He/^4He$ and other isotope ratios (Fig. 6b–d). In
277   contrast, the enriched group ($(La/Sm)_N \geq 2$) deviates from this negative correlation and has
278   relatively scattered $^3He/^4He$ ratios (Fig. 6b–d). Sample DGFB121601 from the southern part of
279   the Fiji Triple Junction segment near the triple junction has an anomalously high $^3He/^4He$ (12.5
280   R_A), that has been duplicated (Table S1). This value is comparable with those of the northern
281   Lau Basin (Lupton et al., 2009, 2012, 2015; Fig. 6).

5 Discussion

5.1. Geochemical heterogeneity

The geochemistry reveals two groups of CSR basalts. Fractional crystallization had a negligible effect on the geochemical differences between the two sample groups, because the large difference in the La/Sm ratios could not have resulted from fractionation of olivine, clinopyroxene, and plagioclase. The variation in K_2O and P_2O_5 between the two groups (Fig. 2)—which are incompatible in olivine, clinopyroxene, and plagioclase—are considered to have resulted from mixing of two melt types; a hydrous–enriched and anhydrous–depleted melt.

The systematic differences in incompatible trace element abundances (Fig. 3) and isotopic compositions (Fig. 5) between the two sample groups can be explained by variation in composition of the mantle beneath the CSR. H_2O contents, $(La/Sm)_N$ ratios and Sr–Nd–Pb isotope ratios co-vary along ridge axis (Fig. 7). Enriched basalts are restricted to the northern segments, whereas the relatively depleted are present throughout the CSR. This implies that mantle heterogeneity is restricted in distribution.

The depleted basalts have H_2O–CO_2 contents that are in the range of MORBs (Dixon et al., 2004), whereas the enriched basalts have H_2O–CO_2 contents similar to Samoan OIBs (Workman et al., 2006; Fig. 4c). Several enriched basalts from the N160 and Fiji Triple Junction segments have higher H_2O contents than the values reported from the southernmost segment (174E; 0.29–0.80 wt.% H_2O; Kendrick et al., 2014), which is located near the active subduction zone. The H_2O-rich nature of the enriched CSR magma is inconsistent with back-arc basin magmatism, in which the degree of melting increases with the H_2O content of mantle. Kelley et al. (2006) noted that the NFB basalts exhibit a weak negative correlation between H_2O contents and melt fraction (F), similar to hotspot-influenced MORBs. Thus, given that the back-arc spreading axis is distal to the active subduction zone, the melts beneath the CSR were dominantly generated by decompression melting rather than H_2O-fluxed melting, and the H_2O enrichment reflects the mantle source and not sub-arc fluids. The enriched CSR basalts have high H_2O contents due to their OIB-like enriched mantle source rather than the sub-arc mantle wedge. This is consistent with no negative Nb-Ta anomalies in the trace element concentration patterns of the basalts.

The mantle heterogeneity in the study area can be assessed in a plot of La/Sm versus Ba/Nb (Fig. 8a). The CSR basalts exhibit mixing between depleted and enriched mantle reservoirs, while the samples from 174E have a subduction input. The enriched group of samples from the northern CSR have high La/Sm and low Ba/Nb ratios that overlap the range for Samoan basalts. These distinctive compositions indicate that the heterogeneity in the mantle beneath the central NFB is intrinsic to upwelling asthenospheric mantle rather than subduction alteration.

A plot of Ti/Y versus Nb/Y (Fig. 8b) demonstrates that there are different types of basalts in the CSR which are emplaced in various tectonic settings. The enriched and depleted sample groups plot in the fields from mid-ocean ridge tholeiitic to within-plate alkaline basalts. Although all of the samples are sub-alkaline basalts (Fig. 2), the enriched samples have relatively high alkali contents and plot close to the boundary for alkaline basalts at a given SiO_2 content. These samples also have trace element compositions consistent with low degrees of melting of mantle peridotite. Thus, the enriched CSR basalts might have been generated from a deep-seated mantle source that was different to DMM.

325   Variation in the depth and degree of mantle melting beneath the study area can be
326 constrained by comparison with the modelled partial melting curves of Baker et al. (1997) for
327 spinel and garnet peridotite on plots of Yb versus La/Yb and La/Sm versus Sm/Yb (Fig. 8c–d).
328 The depleted MORB-like basalts plot on the curve from 5–10% partial melting of spinel
329 lherzolite. The enriched OIB-like CSR basalts can be generated by smaller degrees of melting
330 (3–5%), with a significant proportion (~70%) of the melt derived from garnet-bearing mantle
331 (Fig. 8d). For spinel and garnet stability field transition defined by Robinson & Wood (1998),
332 this implies that the enriched CSR basalts require initial melting that at depth greater than 85 km.

333   In summary, the geochemical heterogeneity of the CSR basalts is the result of regional
334 variations in the mantle source. Melting beneath the northern segments has tapped enriched
335 mantle source, while depleted basalts appear throughout the CSR. The depleted mantle does not
336 have an arc-like signature because the CSR is a mature stage of spreading in the North Fiji back-
337 arc basin.

338   5.2. Origin of the enriched Central Spreading Ridge basalts

339   5.2.1. Samoan mantle plume?

340   Previous studies have suggested that the Samoan mantle plume is the source of the
341 enriched components in the northern NFB and Lau Basin (A. Price et al., 2014, 2017). Chang et
342 al. (2016) and Druken et al. (2014) proposed that toroidal flow of upwelling Samoan mantle
343 plume around a slab edge can account for the enriched, high ^{3}He/^{4}He basalts in the northern Lau
344 Basin and Fiji. A. Price et al. (2014) used this concept to explain the isotopic gradient observed
345 in basalts from the Lau and North Fiji basins, whereby mixing of plume material injected by
346 adiabatic decompression melting with DMM occurs beneath the young back-arc basin crust. The
347 similar volatile compositions of Samoan and enriched CSR basalts might be evidence for the
348 presence of Samoan mantle plume material in the northern NFB mantle.

349   However, several issues remain unresolved with respect to this model. For example, the
350 Samoan mantle plume shows temporal heterogeneity (Jackson et al., 2014) and more constraints
351 are needed to reveal which component is present in the NFB mantle. A. Price et al. (2017)
352 proposed that the enriched isotopic compositions of CSR basalts are similar to those of the Alexa
353 Bank (Hart et al., 2004); the most depleted part of the Upo lineament composition defined by
354 mixing between DMM and elevated ^{3}He/^{4}He common mantle component, FOZO (Focal Zone;
355 Hart et al., 1992) (or "C"; Hanan & Graham, 1996; Jackson et al., 2014). The Sr–Nd isotopic
356 composition of the Alexa Bank samples trends toward the EM1 end-member like the enriched
357 CSR basalts (Fig. 5a). However, most of the enriched CSR samples have more radiogenic Sr and
358 Nd isotopes and less radiogenic ^{206}Pb/^{204}Pb than the Alexa Bank basalts (Fig. 5b–e). The
359 enriched mantle beneath the Alexa Bank is unlikely to be a plausible source of the enriched melts
360 in the northern CSR.

361   A comparison with volcanic rocks from the northern Lau Basin lend credence to the
362 Samoan mantle plume being the source of enriched mantle beneath the northern CSR. The
363 reported data from the Samoan-mantle-plume-influenced back-arc spreading segments in the
364 northern Lau Basin (Lupton et al., 2009; Lytle et al., 2012), Rochambeau Rift and parts of
365 Northwest Lau Spreading Center, are close to the enriched CSR basalts in the Sr-Nd-Pb isotope
366 spaces (Fig. 5a and c). Rest of the Northwest Lau Spreading Center basalts are distinguished
367 from the enriched CSR samples and are similar to the North Fiji Fracture Zone, presenting a
368 depleted back-arc mantle composition shown by Nebel & Arculus (2015) (Fig. 5a).

369   Yet, the absence of a strong correlation between He and Sr–Nd–Pb isotopes, and the
370   dominance of more depleted mantle-like ^{3}He/^{4}He (9 ± 0.4 R$_A$) rather than the high values
371   recorded by the Rochambeau Rift and Northwest Lau Spreading Center basalts (11–30 R$_A$) fail
372   to support the presence of the Samoan mantle plume beneath the NFB (Fig. 6). In fact, mixing
373   between the refractory back-arc mantle and a spatially restricted FOZO component that might
374   originate from the Samoan plume, is suggested to describe their Hf-Nd-noble gas isotope
375   characteristics (Nebel & Arculus, 2015). Degassing of the He from plume mantle melts prior to
376   mixing with melts of depleted upper mantle have been called on to explain a similar observation
377   with Lau Basin basalts (A. Price et al., 2014). While this could explain the DMM-like ^{3}He/^{4}He of
378   the enriched CSR basalts it requires a rather peculiar set of circumstances (i.e., > 99% degassing
379   of helium) that are not common elsewhere enriched mantle heterogeneities melt beneath ridges.
380   As noted in previous studies (Nishio et al., 1998; R. Price et al., 1990), the distinctive features of
381   the enriched CSR basalts require an additional or alternative mantle enrichment process, which
382   can produce the weak EM1-like signature of the enriched basalts emplaced in the central region
383   of the mature back-arc basin.

384   5.2.2. Upper mantle upwelling induced by a stagnant slab in the mantle transition zone

385   We compared published data from adjacent spreading centers and oceanic islands (Fig. 5)
386   to examine the regional variations in the geochemically enriched compositions. Fiji samples
387   showing an obvious subduction input (Fiji island arc tholeiite in Fig. 3) were excluded in the
388   comparison. The OIB-like Fiji and, in particular, South Pandora Ridge samples have the closest
389   geochemical affinities with the enriched CSR basalts (Figs 3 and 5).

390   The Sr–Nd–Pb isotope data reported from sites located between the CSR and Samoa,
391   such as the North Fiji Fracture Zone, Futuna Spreading Center, northeast Peggy Ridge and
392   Futuna volcano, exhibit a trend towards EM2 (Fig. 5). The Alexa Bank, which was derived from
393   mantle affected by the older part of the Samoan mantle plume (i.e., the Upo lineament), was also
394   involved (Fig. 5). These samples are distinct from the enriched CSR basalts and have higher
395   ^{206}Pb/^{204}Pb ratios at given Sr, Nd, ^{207}Pb/^{204}Pb, and ^{208}Pb/^{204}Pb compositions (Fig. 5b–e). Even
396   Rotuma and Manatu seamounts, which are located closer to Samoa than to the Alexa Bank, have
397   moderately enriched isotopic compositions that are distinct from the enriched CSR basalts (Fig.
398   5). Only Wallis Island, close to the present-day Samoan hotspot, and Tripartite Ridge has an
399   EM1-like signature comparable to rejuvenated Samoan volcanic rocks.

400   The Alexa Bank and most of the MORB-like CSR samples plot in the field for MORBs
401   and Samoa (Fig. 9), and have low Ba/Th ratios with respect to the enriched CSR basalts and
402   rejuvenated Samoan volcanic rocks with a EM1-like signature (Fig. 9a). Some of the enriched
403   CSR, South Pandora Ridge, and Fiji basalts are distinct from the Alexa Bank, MORB-like CSR,
404   and NW Lau Basin basalts in Ba/Th-Zr/Th space (Fig. 9b) and have significantly higher Ba/La
405   (Fig. 9c). Through the Principal Component Analysis (PCA) of the selected geochemical proxies,
406   Sr-Nd-Pb-He isotopes and Ba/Th, Ba/Ta, Zr/Hf, Zr/Th and La/Ta, it is clarified that the Ba-rich
407   characteristic of the enriched CSR basalts is much closer to those of rejuvenated Samoa, Wallis
408   and South Pandora Ridge basalts than the shield-stage Samoan lavas which have lower mantle
409   origin (Fig. 10). The enriched CSR, South Pandora Ridge, Wallis, and rejuvenated Samoa
410   samples have high Ba/Th and Ba/Ta ratios and present weak association with the shield-stage
411   Samoan groups of EM2, HIMU, FOZO and DM components. Pitcairn, a representative EM1-
412   type OIB (Eisele et al., 2002), also shows the Ba-rich feature similar to the rejuvenated Samoan
413   lavas, supporting that the feature is inherent nature of EM1 magmatism. Thus, the generation of

414 enriched CSR magma needs to be evaluated from a perspective independent of Samoan plume
415 activity. Furthermore, the PCA result shows that the EM1-signature in the CSR and the
416 rejuvenated Samoa is distinguished from typical EM1, Pitcairn, associated with plume activity
417 (Table S3 and Figure S1). Therefore, we consider that the CSR lavas are a kind of non-plume
418 enriched magmatism together with the rejuvenated Samoan lavas.

419   Johnson and Sinton (1990) stated that the enriched CSR basalts are relatively young and
420 correspond to alkaline volcanism at the South Pandora Ridge, Wallis, Rotuma and Fiji Islands.
421 They suspected the cause of that enriched and young magmatism is a kind of rejuvenated
422 volcanism that occurred at a weak zone formed by previous tectonic stress, induced by isolated
423 upwelling of the enriched mantle source. Jackson et al. (2010) noted that volcanic rocks from
424 Wallis Island show geochemical affinities to rejuvenated Samoan volcanic rocks (Figs. 5, 9, and
425 10), and suggested that they formed in response to recent tectonic stresses. Reinhard et al. (2019)
426 also suggested that the rejuvenated (EM1-type) Samoan lavas initiated at ~25 ka may be a result
427 of "petit spot" volcanism induced by tectonic uplift outboard of the Tonga Trench. Considering
428 the mechanism and timing of the initiation of rejuvenated Samoan volcanism, and the distance
429 from the CSR, the southward flow of melts preserving the EM1 component from the rejuvenated
430 Samoa to the central NFB is unlikely to be the mantle source of the enriched CSR basalts. More
431 likely that an isolated and local mantle enrichment process may explain the distinctive OIB-like
432 signature of the enriched northern CSR, South Pandora Ridge, and Fiji basalts.

433   The distinct high Ba/Th and Ba/Ta ratios of the enriched CSR basalts (Fig 9 and 10) can
434 be a result of the process supplying substantial fluid components from slabs. Supporting this, the
435 CSR basalts, and Fijian arc basalts, have elevated H_2O/Ce and Ba/Th ratios (Fig. 11). However,
436 trace element patterns of the CSR basalts (i.e. no depletion of HFSE such as Nb and Ta, Fig. 3)
437 cannot be attributed to the typical sub-arc mantle, Instead, the Ba-rich characteristic of the
438 enriched CSR basalts is similar to those of the Gaussberg lamproite in Antarctica and the
439 Cenozoic alkaline basalts in NE China, which is considered to have originated from the
440 metasomatized K-hollandite in the ancient stagnant slab in the MTZ (Murphy et al., 2002;
441 Kuritani et al., 2011; Chen et al., 2017). Thus, we propose that dehydrated and altered oceanic
442 crust and/or sediments were involved in their source region at depth.

443   Additionally, the recycled ancient slab component is the most plausible source for the
444 EM1-like isotopic signature of the CSR basalts among the several scenarios suggested as the
445 origin of EM1. The recent slab materials released into the MTZ are too young (ca. 4 Ma) to
446 generate the significant radiogenic Sr and Nd isotope composition of the enriched CSR basalts.
447 Although the numerical models attested that the recent stagnation process could form the molten
448 mantle above the slab edge by interaction with the hydrous MTZ (Long et al., 2019; Yang &
449 Faccenda, 2020), the partial melting of mineral phases comprising the upper mantle cannot
450 induce the enriched isotopic composition (Kuritani et al., 2011). On the other hand, the ancient
451 subducted slab can give the EM1-like isotopic signature in addition to the Ba-rich property to the
452 hydrous MTZ-derived magmatism (Murphy et al., 2002; Kuritani et al., 2011; Wang et al., 2017).
453 The long-term (ca. 2 Ga) recycled bulk oceanic crust components (basalt + sediment) calculated
454 by Kimura et al. (2016) can describe the enriched CSR samples with the component in a range of
455 20–30% of sediment (Fig. 5). Long et al. (2019) presented a geodynamic model substantiating
456 upwelling developed within a few million years and argued that they are delivered to the base of
457 the lithosphere by small-scale convection. Consequently, the recent slab stagnation beneath the

458 NFB, triggering self-buoyant hydrous upwelling from the MTZ depth, may deliver the ancient
459 recycled components into the lithospheric mantle.

460   The enriched CSR samples contain a large proportion of garnet peridotite-derived melt
461 compared with the depleted CSR or the other back-arc samples. Based on this, the enriched CSR
462 samples were generated near the garnet–spinel mantle transition zone (~80 km depth). Zhang and
463 Pysklywec (2006) proposed that hot, buoyant, upper mantle upwelling occurs at depths of 70–
464 120 km beneath the NFB, which can explain the anomalously shallow seafloor in the region.
465 This depth range coincides with that of the garnet–spinel mantle transition in the lower oceanic
466 lithosphere. Therefore, the buoyant material may be mantle ascending from the edge of a
467 stagnant slab, which generated the garnet signature in the magmas emplaced along the ridge axis,
468 due to the melting of the adjacent lower oceanic lithosphere or recycling of stagnant slab
469 materials.

470   As such, we propose a model that involves mantle upwelling from the hydrated MTZ to
471 explain the EM1-like signature and presence of altered lower oceanic crustal components in
472 magmatism in this trench-distal back-arc basin. The ascending material supplied the volatiles and
473 was responsible for the distinctive enriched isotopic and trace element features of the back-arc
474 magmatism in the northern CSR and South Pandora Ridge. These features can be distinguished
475 from shield-stage Samoan volcanic rocks by their high Ba/Th and Ba/Ta ratios, which are
476 indicative of the recycling of oceanic slab components. Primordial helium from the MTZ
477 (Timmerman et al., 2019) may be responsible for the slightly elevated ^{3}He/^{4}He ratios in the
478 upper mantle beneath the NFB (Fig. 6). Our model for the source of the enriched OIB-like
479 basalts in the northern CSR and South Pandora Ridge can explain features that were not fully
480 addressed by the lateral flow of the Samoan mantle plume beneath the NFB.

481   5.3. Geodynamic implications for enriched magmatism in the North Fiji Basin

482   In the NFB, clusters of deep earthquakes, unrelated to back-arc extension, have been
483 detected at 500–660 km beneath the northwestern and western NFB (Chen & Brudzinski, 2001;
484 Richards et al., 2011; Van der Hilst, 1995). It is widely thought that stagnant slab fragments exist
485 at depths of 410–660 km beneath the NFB, although whether they detached from the Australian
486 (Richards et al., 2011) or Pacific (Chang et al., 2016) plate is unclear. Richard et al. (2011)
487 suggested the existence of two different slabs, the detached Australian plate and the down-going
488 Pacific slab, in the MTZ depth beneath the NFB. At 3–4 Ma, the east-dipping Australian plate
489 was completely torn, generating the slab window in the eastern CSR, and came into collision
490 with the east-dipping Pacific slab underneath the Fiji platform. Based on a map showing the
491 spatial distribution of the detached slabs (Chen & Brudzinski, 2001; Richards et al., 2011), the
492 Fiji Triple Junction and N15 segments are located parallel to the edge of the eastern slab, the
493 N160 segment lies above a slab window in the western CSR, and the SPR lies partly over the
494 western slab (Fig. 1c). Faccenna et al. (2010) noted that focused mantle upwelling occurs at the
495 edge of slabs in the MTZ the deep earthquakes may represent deformation and/or dehydration
496 reactions in detached flat-lying slabs in the MTZ. Thus, the spatial affinity between the stagnant
497 slabs and the location of distinctive enriched magmatism in the CSR and SPR supports our
498 model.

499   Figure 12 shows our stagnant slab model for the EM1-like OIB magmatism in the
500 northern CSR. The positions of hydrous mantle and molten mantle are according to the model of
501 Yang & Faccenda (2020). It demonstrates the mantle upwelling from the MTZ depth by

dehydration of stagnant slab, generating three main melts located (1) at the back of dipping slab that might be related to petit-spot volcanism, (2) beneath the stagnant slab, and (3) above the slab-edge, respectively. We consider that the third type of melts corresponds to the source of enriched CSR basalts. Based on the interpretation of combined P-wave tomography and seismicity of the NFB (Van der Hilst, 1995), a low velocity zone (LVZ) was detected just atop and along the stagnant slab, which we considered as a hydrous mantle shown in Figure 12. And the other low velocity zone located at shallow upper mantle depth above the edge of stagnant slab was interpreted as a source melts (or mantle) of geochemically enriched component observed in the northern CSR and the South Pandora Ridge.

During stagnation in the MTZ, breakdown and deformation of the slab can supply water to the ambient mantle. Slab detachment may have accelerated the decomposition and hydration of the MTZ along the slab edge and window located just beneath the Fiji Triple Junction, N15, and N160 segments. In the atop the hydrated MTZ, melting occurred due to the increased water content, which generated enriched mantle with recycled oceanic crust and sediment components. This enriched mantle ascended into the asthenosphere to depths of 70–120 km by small-scale convection and then localized OIB-like melts were emplaced beneath the melting regime of the DMM at the FTJ or lower boundary of the existing oceanic lithosphere. Finally, mixing of melts from the DMM and OIB mantle produced the weak EM1-like signatures and N-MORB compositions in the northern NFB.

6 Conclusions

Spatial compositional variations of basalts erupted along back-arc spreading ridges in the NFB require mixing between DMM and a moderately enriched mantle component with an EM1-like signature. The MORB-type composition is dominant in the southern ridge and NS segment, and was sourced from DMM during the mature back-arc stage. The enriched basalts from the northern NFB are characterized by an a weak EM1 isotopic signature that is distinct from the shield-stage volcanoes produced by the Samoan mantle plume. Geochemical features—such as high H_2O contents (0.63–1.22 wt.%) and Ba/Th ratios—of the OIB-like NFB basalts with EM1 signatures are similar to those of intraplate magmatism derived by mantle upwelling from the hydrous MTZ. A large amount of garnet peridotite-derived melt in the OIB-like NFB basalts requires deep melting beneath the central NFB, or recycling of a slab in the MTZ. Slightly elevated $^3He/^4He$ ratios compared with typical MORB mantle reveal the upward flow of mantle with primordial helium. Thus, we propose that the EM1-like magmas generated at trench- and plume-distal spreading ridges were associated with upwelling hydrous mantle above the edge of a stagnant slab.

545

References

Aggrey, K. E., Muenow, D. W., & Sinton, J. M. (1988). Volatile abundances in submarine glasses from the North Fiji and Lau back-arc basins. *Geochimica et Cosmochimica Acta, 52*(10), 2501–2506. https://doi.org/10.1016/0016-7037(88)90308-0

Arevalo Jr, R., & McDonough, W. F. (2010). Chemical variations and regional diversity observed in MORB. *Chemical Geology, 271*(1–2), 70–85. https://doi.org/10.1016/j.chemgeo.2009.12.013

Auzende, J. M., Lafoy, Y., & Marsset, B. (1988). Recent geodynamic evolution of the North Fiji Basin (Southwest Pacific). *Geology, 16*(10), 925–929. https://doi.org/10.1130/0091-7613(1988)016<0925:RGEOTN>2.3.CO;2

Baker, J., Menzies, M., Thirlwall, M., & Macpherson, C. (1997). Petrogenesis of Quaternary intraplate volcanism, Sana'a, Yemen: implications for plume-lithosphere interaction and polybaric melt hybridization. *Journal of Petrology*, 38(10), 1359–1390. https://doi.org/10.1093/petroj/38.10.1359

Bijwaard, H., Spakman, W., & Engdahl, E. (1998). Closing the gap between regional and global travel time tomography. *Journal of Geophysical Research, 1033*, 30055–30078. http://doi.org/10.1029/98JB02467

Byers, C. D., Muenow, D. W., & Garcia, M. O. (1983). Volatiles in basalts and andesites from the Galapagos Spreading Center, 85° to 86°W. *Geochimica et Cosmochimica Acta, 47*(9), 1551–1558. https://doi.org/10.1016/0016-7037(83)90181-3

Carracedo, A., Rodés, Á., Smellie, J., & Stuart, F. (2019). Episodic erosion in West Antarctica inferred from cosmogenic [3]He and [10]Be in olivine from Mount Hampton. *Geomorphology, 327*, 438–445. https://doi.org/10.1016/j.geomorph.2018.11.019

Chang, S. J., Ferreira, A. M., & Faccenda, M. (2016). Upper- and mid-mantle interaction between the Samoan plume and the Tonga-Kermadec slabs. *Nature Communications, 7*, 10799. https://doi.org/10.1038/ncomms10799

Chen, H., Xia, Q.-K., Ingrin, J., Deloule, E., & Bi, Y. (2017). Heterogeneous source components of intraplate basalts from NE China induced by the ongoing Pacific slab subduction. *Earth and Planetary Science Letters, 459*, 208–220. https://doi.org/10.1016/j.epsl.2016.11.030

Chen, W.-P., & Brudzinski, M. R. (2001). Evidence for a Large-Scale Remnant of Subducted Lithosphere Beneath Fiji. *Science, 292*(5526), 2475–2479. http://doi.org/10.1126/science.292.5526.2475

Danyushevsky, L. V., & Plechov, P. (2011). Petrolog3: Integrated software for modeling crystallization processes. *Geochemistry, Geophysics, Geosystems, 12*(7), Q07021. https://doi.org/10.1029/2011GC003516

Dixon, J. E., Dixon, T. H., Bell, D. R., & Malservisi, R. (2004). Lateral variation in upper mantle viscosity: role of water. *Earth and Planetary Science Letters, 222*(2), 451–467. https://doi.org/10.1016/j.epsl.2004.03.022

584   Dixon, J. E., Stolper, E., & Delaney, J. R. (1988). Infrared spectroscopic measurements of CO_2
585   and H_2O in Juan De Fuca Ridge basaltic glasses. *Earth and Planetary Science Letters, 90*(1), 87–
586   104. https://doi.org/10.1016/0012-821X(88)90114-8

587   Dixon, J. E., & Stolper, E. M. (1995). An experimental study of water and carbon dioxide
588   solubilities in mid-ocean ridge basaltic liquids. Part II: applications to degassing. *Journal of*
589   *Petrology, 36*(6), 1633–1646. https://doi.org/10.1093/oxfordjournals.petrology.a037268

590   Druken, K. A., Kincaid, C., Griffiths, R. W., Stegman, D. R., & Hart, S. R. (2014). Plume–slab
591   interaction: The Samoa–Tonga system. *Physics of the Earth and Planetary Interiors, 232*, 1–14.
592   http://doi.org/10.1016/j.pepi.2014.03.003

593   Eisele, J., Sharma, M., Galer, S. J. G., Blichert-Toft, J., Devey, C. W., & Hofmann, A. W. (2002).
594   The role of sediment recycling in EM-1 inferred from Os, Pb, Hf, Nd, Sr isotope and trace
595   element systematics of the Pitcairn hotspot. *Earth and Planetary Science Letters, 196*(3), 197-
596   212. https://doi.org/10.1016/S0012-821X(01)00601-X

597   Eissen, J.-P., Nohara, M., Cotten, J., & Hirose, K. (1994). North Fiji Basin basalts and their
598   magma sources: Part I. Incompatible element constraints. *Marine Geology, 116*(1–2), 153–178.
599   https://doi.org/10.1016/0025-3227(94)90174-0

600   Eissen, J. -P., Lefevre, C., Maillet, P., Morvan, G., & Nohara, M. (1991). Petrology and
601   Geochemistry of the Central North Fiji Basin Spreading Centre (Southwest Pacific) between
602   16°S and 22°S. *Marine Geology, 98*(2–4), 201–239. http://doi.org/10.1016/0025-3227(91)90104-
603   C

604   Faccenna, C., Becker, T. W., Lallemand, S., Lagabrielle, Y., Funiciello, F., & Piromallo, C.
605   (2010). Subduction-triggered magmatic pulses: A new class of plumes? *Earth and Planetary*
606   *Science Letters, 299*(1–2), 54–68. http://doi.org/10.1016/j.epsl.2010.08.012

607   Farley, K., Craig, H., Hart, S. R., Hauri, E., Oschmann, L., & Whitehead, J. (1992). Mantle
608   plumes and mantle sources. *Science, 258*(5083), 821–823.

609   Gale, A., Dalton, C. A., Langmuir, C. H., Su, Y., & Schilling, J.-G. (2013). The mean
610   composition of ocean ridge basalts. *Geochemistry, Geophysics, Geosystems, 14*(3), 489–518.
611   http://doi.org/10.1029/2012gc004334.

612   Garel, E., Lagabrielle, Y., & Pelletier, B. (2005). Abrupt axial variations along the slow to ultra-
613   slow spreading centers of the northern North Fiji Basin (SW Pacific): Evidence for short wave
614   heterogeneities in a back-arc mantle. *Marine Geophysical Researches, 24*(3–4), 245–263.
615   http://doi.org/10.1007/s11001-004-1060-y

616   Gorring, M., Singer, B., Gowers, J., & Kay, S. M. (2003). Plio–Pleistocene basalts from the
617   Meseta del Lago Buenos Aires, Argentina: evidence for asthenosphere–lithosphere interactions
618   during slab window magmatism. *Chemical Geology, 193*(3–4), 215–235.
619   https://doi.org/10.1016/S0009-2541(02)00249-8

620   Graham, D. W. (2002). Noble gas isotope geochemistry of mid-ocean ridge and ocean island
621   basalts: Characterization of mantle source reservoirs. *Noble Gases in Geochemistry and*
622   *Cosmochemistry, 47*(1), 247–317. http://doi.org/10.2138/rmg.2002.47.8

623 Hanan, B. B., & Graham, D. W. (1996). Lead and Helium Isotope Evidence from Oceanic
624 Basalts for a Common Deep Source of Mantle Plumes. *Science, 272*(5264), 991–995.
625 http://doi.org/10.1126/science.272.5264.991

626 Hart, S. R. (1984). A large-scale isotope anomaly in the Southern Hemisphere mantle. *Nature,*
627 *309*, 753. http://doi.org/10.1038/309753a0

628 Hart, S. R., Hauri, E., Oschmann, L., & Whitehead, J. (1992). Mantle plumes and entrainment:
629 isotopic evidence. *Science, 256*(5056), 517–520. http://doi.org/10.1126/science.256.5056.517

630 Hart, S. R., Coetzee, M., Workman, R. K., Blusztajn, J., Johnson, K. T. M., Sinton, J. M., . . .
631 Hawkins, J. W. (2004). Genesis of the Western Samoa seamount province: age, geochemical
632 fingerprint and tectonics. *Earth and Planetary Science Letters, 227*(1–2), 37–56.
633 http://doi.org/10.1016/j.epsl.2004.08.005

634 Jackson, M. G., Hart, S. R., Konter, J. G., Koppers, A. A. P., Staudigel, H., Kurz, M. D., . . .
635 Sinton, J. M. (2010). Samoan hot spot track on a "hot spot highway": Implications for mantle
636 plumes and a deep Samoan mantle source. *Geochemistry, Geophysics, Geosystems, 11*(12),
637 Q12009. http://doi.org/10.1029/2010gc003232

638 Jackson, M. G., Hart, S. R., Konter, J. G., Kurz, M. D., Blusztajn, J., & Farley, K. A. (2014).
639 Helium and lead isotopes reveal the geochemical geometry of the Samoan plume. *Nature,*
640 *514(7522)*, 355–358. http://doi.org/10.1038/nature13794

641 Johnson, K. T., & Sinton, J. M. (1990). Petrology, tectonic setting, and the formation of back-arc
642 basin basalts in the North Fiji Basin. *Geological Evolution and Hydrothermal Activity in the Lau*
643 *and North Fiji Basins, Southwest Pacific Ocean, Results of Sonne Cruise SO, 35*, 517–545.

644 Kelley, K. A., Plank, T., Grove, T. L., Stolper, E. M., Newman, S., & Hauri, E. (2006). Mantle
645 melting as a function of water content beneath back-arc basins. *Journal of Geophysical*
646 *Research-Solid Earth, 111*(B9), B09208. http://doi.org/10.1029/2005jb003732

647 Kendrick, M. A., Arculus, R. J., Danyushevsky, L. V., Kamenetsky, V. S., Woodhead, J. D., &
648 Honda, M. (2014). Subduction-related halogens (Cl, Br and I) and H_2O in magmatic glasses from
649 Southwest Pacific Backarc Basins. *Earth and Planetary Science Letters, 400*, 165–176.
650 http://doi.org/10.1016/j.epsl.2014.05.021

651 Kim, J., Pak, S.-J., Moon, J.-W., Lee, S.-M., Oh, J., & Stuart, F. M. (2017). Mantle heterogeneity
652 in the source region of mid-ocean ridge basalts along the northern Central Indian Ridge (8°S-
653 17°S). *Geochemistry, Geophysics, Geosystems, 18*(4), 1419–1434.
654 http://doi.org/10.1002/2016gc006673

655 Kimura, J.-I., Gill, J. B., Skora, S., van Keken, P. E., & Kawabata, H. (2016). Origin of
656 geochemical mantle components: Role of subduction filter. *Geochemistry, Geophysics,*
657 *Geosystems, 17*(8), 3289-3325. http://doi.org/10.1002/2016gc006343

658 Konter, J. G., & Jackson, M. G. (2012). Large volumes of rejuvenated volcanism in Samoa:
659 Evidence supporting a tectonic influence on late-stage volcanism. *Geochemistry, Geophysics,*
660 *Geosystems, 13*(6), Q0AM04. http://doi.org/10.1029/2011gc003974

661 Kuritani, T., Ohtani, E., & Kimura, J.-I. (2011). Intensive hydration of the mantle transition zone
662 beneath China caused by ancient slab stagnation. *Nature Geoscience, 4*(10), 713–716.
663 http://doi.org/10.1038/ngeo1250

Kuritani, T., Xia, Q.-K., Kimura, J.-I., Liu, J., Shimizu, K., Ushikubo, T., . . . Yoshimura, S. (2019). Buoyant hydrous mantle plume from the mantle transition zone. *Scientific Reports, 9*(1), 6549. http://doi.org/10.1038/s41598-019-43103-y

Kurz, M., Jenkins, W., & Hart, S. (1982). Helium isotopic systematics of oceanic islands and mantle heterogeneity. *Nature, 297*(5861), 43–47. https://doi.org/10.1038/297043a0

Lafoy, Y., Auzende, J. M., Ruellan, E., Huchon, P., & Honza, E. (1990). The 16°40′S triple junction in the North Fiji Basin (SW Pacific). *Marine Geophysical Researches, 12*(4), 285–296. http://doi.org/10.1007/bf02428199

Lang, D. C., Bailey, I., Wilson, P. A., Beer, C. J., Bolton, C. T., Friedrich, O., . . . Milton, J. A. (2014). The transition on North America from the warm humid Pliocene to the glaciated Quaternary traced by eolian dust deposition at a benchmark North Atlantic Ocean drill site. *Quaternary Science Reviews, 93*, 125-141. https://doi.org/10.1016/j.quascirev.2014.04.005

Long, X., Ballmer, M. D., Córdoba, A. M.-C., & Li, C.-F. (2019). Mantle melting and intraplate volcanism due to self-buoyant hydrous upwellings from the stagnant slab that are conveyed by small-scale convection. *Geochemistry, Geophysics, Geosystems, 20*, 4972– 4997. https://doi.org/10.1029/2019GC008591

Lupton, J., Rubin, K. H., Arculus, R., Lilley, M., Butterfield, D., Resing, J., . . . Embley, R. (2015). Helium isotope, $C/^3He$, and Ba-Nb-Ti signatures in the northern Lau Basin: Distinguishing arc, back-arc, and hotspot affinities. *Geochemistry, Geophysics, Geosystems, 16*(4), 1133–1155. http://doi.org/10.1002/2014gc005625

Lupton, J. E., Arculus, R. J., Evans, L. J., & Graham, D. W. (2012). Mantle hotspot neon in basalts from the Northwest Lau Back-arc Basin. *Geophysical Research Letters, 39*(8), L08308. http://doi.org/10.1029/2012gl051201

Lupton, J. E., Arculus, R. J., Greene, R. R., Evans, L. J., & Goddard, C. I. (2009). Helium isotope variations in seafloor basalts from the Northwest Lau Backarc Basin: Mapping the influence of the Samoan hotspot. *Geophysical Research Letters, 36*(17), L17313. http://doi.org/10.1029/2009gl039468

Lytle, M. L., Kelley, K. A., Hauri, E. H., Gill, J. B., Papia, D., & Arculus, R. J. (2012). Tracing mantle sources and Samoan influence in the northwestern Lau back-arc basin. *Geochemistry, Geophysics, Geosystems, 13*(10), Q10019. http://doi.org/10.1029/2012gc004233

Martin, A. K. (2013). Double-saloon-door tectonics in the North Fiji Basin. *Earth and Planetary Science Letters, 374*, 191–203. http://doi.org/10.1016/j.epsl.2013.05.041

Martin, A. K. (2014). Concave slab out board of the Tonga subduction zone caused by opposite toroidal flows under the North Fiji Basin. *Tectonophysics, 622*, 56–61. http://doi.org/10.1016/j.tecto.2014.02.009

Marty, B., & Zimmermann, L. (1999). Volatiles (He, C, N, Ar) in mid-ocean ridge basalts: assesment of shallow-level fractionation and characterization of source composition. *Geochimica et Cosmochimica Acta, 63*(21), 3619–3633. http://doi.org/10.1016/s0016-7037(99)00169-6

Matsuda, J., Matsumoto, T., Sumino, H., Nagao, K., Yamamoto, J., Miura, Y., . . . Sano, Y. (2002). The $^3He/^4He$ ratio of the new internal He Standard of Japan (HESJ*). Geochemical Journal, 36*(2), 191–195. https://doi.org/10.2343/geochemj.36.191

705 McDonough, W. F., & Sun, S.-S. (1995). The composition of the Earth. *Chemical Geology,*
706 *120*(3–4), 223–253. https://doi.org/10.1016/0009-2541(94)00140-4

707 Meffre, S., & Crawford, A. J. (2001). Collision tectonics in the New Hebrides arc (Vanuatu).
708 *Island Arc, 10*(1), 33–50. http://doi.org/DOI 10.1046/j.1440-1738.2001.00292.x

709 Morgan, W. J. (1971). Convection plumes in the lower mantle. *Nature, 230*(5288), 42–43.
710 https://doi.org/10.1038/230042a0

711 Murphy, D. T., Collerson, K. D., & Kamber, B. S. (2002). Lamproites from Gaussberg,
712 Antarctica: Possible Transition Zone Melts of Archaean Subducted Sediments. *Journal of*
713 *Petrology, 43*(6), 981-1001. doi:10.1093/petrology/43.6.981

714 Nebel, O., & Arculus, R. J. (2015). Selective ingress of a Samoan plume component into the
715 northern Lau backarc basin. *Nature Communications, 6*, 6554.
716 https://doi.org/10.1038/ncomms7554

717 Newman, S., Stolper, E., & Stern, R. (2000). H_2O and CO_2 in magmas from the Mariana arc and
718 back arc systems. *Geochemistry, Geophysics, Geosystems, 1*(5), 1013. http://doi.or
719 g/10.1029/1999gc000027

720 Nishio, Y., Sasaki, S., Gamo, T., Hiyagon, H., & Sano, Y. (1998). Carbon and helium isotope
721 systematics of North Fiji Basin basalt glasses: carbon geochemical cycle in the subduction zone.
722 *Earth and Planetary Science Letters, 154*(1–4), 127–138. http://doi.org/10.1016/S0012-
723 821x(97)00187-8

724 Nohara, M., Hirose, K., Eissen, J.-P., Urabe, T., & Joshima, M. (1994). The North Fiji Basin
725 basalts and their magma sources: Part II. Sr-Nd isotopic and trace element constraints. *Marine*
726 *Geology, 116*(1–2), 179–195. https://doi.org/10.1016/0025-3227(94)90175-9

727 Okal, E. A., & Kirby, S. H. (1998). Deep earthquakes beneath the Fiji Basin, SW Pacific: Earth's
728 most intense deep seismicity in stagnant slabs. *Physics of the Earth and Planetary Interiors,*
729 *109*(1–2), 25–63. https://doi.org/10.1016/S0031-9201(98)00116-2

730 Okino, K., Ando, M., Kaneshima, S., & Hirahara, K. (1989). The horizontally lying slab.
731 *Geophysical Research Letters, 16*(9), 1059–1062. http://doi.org/10.1029/GL016i009p01059

732 Özdemir, Y., & Güleç, N. (2014). Geological and geochemical evolution of the Quaternary
733 Süphan Stratovolcano, Eastern Anatolia, Turkey: evidence for the lithosphere–asthenosphere
734 interaction in post-collisional volcanism. *Journal of Petrology, 55*(1), 37–62.
735 https://doi.org/10.1093/petrology/egt060

736 Pearce, J. A. (1982). Trace element characteristics of lavas from destructive plate boundaries.
737 In R. S. Thorpe (Eds.), *Orogenic andesites and related rocks* (pp. 528–548). Chichester, England:
738 John Wiley and Sons.

739 Pearce, J. A., Kempton, P. D., & Gill, J. B. (2007). Hf–Nd evidence for the origin and
740 distribution of mantle domains in the SW Pacific. *Earth and Planetary Science Letters, 260*(1–2),
741 98–114. http://doi.org/10.1016/j.epsl.2007.05.023

742 Pelletier, B., Calmant, S., & Pillet, R. (1998). Current tectonics of the Tonga–New Hebrides
743 region. *Earth and Planetary Science Letters, 164*(1–2), 263–276. https://doi.org/10.1016/S0012-
744 821X(98)00212-X

Price, A. A., Jackson, M. G., Blichert-Toft, J., Blusztajn, J., Conatser, C. S., Konter, J. G., . . . Kurz, M. D. (2016). Geochemical evidence in the northeast Lau Basin for subduction of the Cook-Austral volcanic chain in the Tonga Trench. *Geochemistry, Geophysics, Geosystems, 17*(5), 1694–1724. http://doi.org/10.1002/2015gc006237

Price, A. A., Jackson, M. G., Blichert-Toft, J., Kurz, M. D., Gill, J., Blusztajn, J., . . . Arculus, R. (2017). Geodynamic implications for zonal and meridional isotopic patterns across the northern Lau and North Fiji Basins. *Geochemistry, Geophysics, Geosystems, 18*(3), 1013–1042. http://doi.org/10.1002/2016gc006651

Price, A. A., Jackson, M. G., Blichert-Toft, J., Hall, P. S., Sinton, J. M., Kurz, M. D., & Blusztajn, J. (2014). Evidence for a broadly distributed Samoan-plume signature in the northern Lau and North Fiji Basins. *Geochemistry, Geophysics, Geosystems, 15*(4), 986–1008. https://doi.org/10.1002/2013GC005061

Price, R. C., Johnson, L., & Crawford, A. (1990). Basalts of the North Fiji Basin: the generation of back arc basin magmas by mixing of depleted and enriched mantle sources. *Contributions to Mineralogy and Petrology, 105*(1), 106–121. https://doi.org/10.1016/0025-3227(91)90105-D.

Price, R. C., & Kroenke, L. W. (1991). Tectonics and magma genesis in the northern North Fiji Basin. *Marine Geology, 98*(2), 241–258. https://doi.org/10.1016/0025-3227(91)90105-D

Reinhard, A. A., Jackson, M. G., Blusztajn, J., Koppers, A. A. P., Simms, A. R., & Konter, J. G. (2019). "Petit spot" rejuvenated volcanism superimposed on plume-derived Samoan shield volcanoes: Evidence from a 645-m drill core from Tutuila Island, American Samoa. *Geochemistry, Geophysics, Geosystems, 20*(3), 1485–1507. http://doi.org/10.1029/2018gc007985

Richards, S., Holm, R., & Barber, G. (2011). When slabs collide: A tectonic assessment of deep earthquakes in the Tonga-Vanuatu region. *Geology, 39*(8), 787–790. http://doi.org/10.1130/g31937.1

Robinson, J. A. C., & Wood, B. J. (1998). The depth of the spinel to garnet transition at the peridotite solidus. *Earth and Planetary Science Letters, 164*(1–2), 277–284. https://doi.org/10.1016/S0012-821X(98)00213-1

Schellart, W. P., Lister, G. S., & Toy, V. G. (2006). A Late Cretaceous and Cenozoic reconstruction of the Southwest Pacific region: Tectonics controlled by subduction and slab rollback processes. *Earth-Science Reviews, 76*(3–4), 191–233. http://doi.org/10.1016/j.earscirev.2006.01.002

Selvaggi, G., & Chiarabba, C. (1995). Seismicity and P-wave velocity image of the Southern Tyrrhenian subduction zone. *Geophysical Journal International, 121*(3), 818–826. https://doi.org/10.1111/j.1365-246X.1995.tb06441.x

Stolper, E. (1982). The speciation of water in silicate melts. *Geochimica et Cosmochimica Acta, 46*(12), 2609–2620. https://doi.org/10.1016/0016-7037(82)90381-7

Stuart, F. M., Ellam, R. M., Harrop, P. J., Fitton, J. G., & Bell, B. R. (2000). Constraints on mantle plumes from the helium isotopic composition of basalts from the British Tertiary Igneous Province. *Earth and Planetary Science Letters, 177*(3–4), 273–285. http://doi.org/10.1016/S0012-821x(00)00050-9

786 Tanaka, T., Togashi, S., Kamioka, H., Amakawa, H., Kagami, H., Hamamoto, T., . . . Dragusanu,
787 C. (2000). JNdi-1: a neodymium isotopic reference in consistency with LaJolla neodymium.
788 *Chemical Geology, 168*(3), 279-281. https://doi.org/10.1016/S0009-2541(00)00198-4

789 Taylor, R. N., Ishizuka, O., Michalik, A., Milton, J. A., & Croudace, I. W. (2015). Evaluating the
790 precision of Pb isotope measurement by mass spectrometry. *Journal of Analytical Atomic*
791 *Spectrometry, 30*(1), 198–213. http://doi.org/10.1039/c4ja00279b

792 Timmerman, S., Honda, M., Burnham, A. D., Amelin, Y., Woodland, S., Pearson, D. G., . . .
793 Tohver, E. (2019). Primordial and recycled helium isotope signatures in the mantle transition
794 zone. *Science, 365*(6454), 692-694. http://doi.org/10.1126/science.aax5293

795 Todd, E., Gill, J. B., & Pearce, J. A. (2012). A variably enriched mantle wedge and contrasting
796 melt types during arc stages following subduction initiation in Fiji and Tonga, southwest Pacific.
797 *Earth and Planetary Science Letters, 335–336*, 180–194.
798 https://doi.org/10.1016/j.epsl.2012.05.006

799 Van der Hilst, R. (1995). Complex morphology of subducted lithosphere in the mantle beneath
800 the Tonga trench. *Nature, 374*, 154–157. https://doi.org/10.1038/374154a0

801 Wang, X.-J., Chen, L.-H., Hofmann, A. W., Mao, F.-G., Liu, J.-Q., Zhong, Y., . . . Yang, Y.-H.
802 (2017). Mantle transition zone-derived EM1 component beneath NE China: Geochemical
803 evidence from Cenozoic potassic basalts. *Earth and Planetary Science Letters, 465*, 16–28.
804 https://doi.org/10.1016/j.epsl.2017.02.028

805 Wharton, M., Hathway, B., & Colley, H. (1994). Volcanism associated with extension in an
806 Oligocene—Miocene arc, southwestern Viti Levu, Fiji. *Geological Society, London, Special*
807 *Publications, 81*(1), 95-114. https://doi.org/10.1144/GSL.SP.1994.081.01.06

808 Workman, R. K., & Hart, S. R. (2005). Major and trace element composition of the depleted
809 MORB mantle (DMM). *Earth and Planetary Science Letters, 231*(1–2), 53–72.
810 http://doi.org/10.1016/j.epsl.2004.12.005

811 Workman, R. K., Hauri, E., Hart, S. R., Wang, J., & Blusztajn, J. (2006). Volatile and trace
812 elements in basaltic glasses from Samoa: Implications for water distribution in the mantle. *Earth*
813 *and Planetary Science Letters, 241*(3–4), 932–951. http://doi.org/10.1016/j.epsl.2005.10.028

814 Yang, J., & Faccenda, M. (2020). Intraplate volcanism originating from upwelling hydrous
815 mantle transition zone. *Nature, 579*(7797), 88–91. http://doi.org/10.1038/s41586-020-2045-y

816 Yuan, H., Yuan, W., Cheng, C., Liang, P., Liu, X., Dai, M., . . . Lai, S. (2016). Evaluation of lead
817 isotope compositions of NIST NBS 981 measured by thermal ionization mass spectrometer and
818 multiple-collector inductively coupled plasma mass spectrometer. *Solid Earth Sciences, 1*(2), 74-
819 78. https://doi.org/10.1016/j.sesci.2016.04.001

820 Yuan, L., Zhang, X., Xue, F., & Liu, F. (2016). Juvenile crustal recycling in an accretionary
821 orogen: Insights from contrasting Early Permian granites from central Inner Mongolia, North
822 China. *Lithos, 264*, 524-539. https://doi.org/10.1016/j.lithos.2016.09.017

823 Zhang, N., & Pysklywec, R. N. (2006). Role of mantle flow at the North Fiji Basin: Insights
824 from anomalous topography. *Geochemistry, Geophysics, Geosystems, 7*(12), Q12002.
825 http://doi.org/10.1029/2006gc001376

826 Zindler, A., & Hart, S. R. (1986). Chemical geodynamics. *Annual Review of Earth and Planetary*
827 *Sciences, 14*(1), 493-571. https://doi.org/10.1146/annurev.ea.14.050186.002425

828

829 **Figure 1.** (a) Regional tectonic map of the North Fiji Basin (NFB) and adjacent areas. The NFB
830 is bordered by the New Hebrides Trench to the west and a fossil trench (i.e. the Vitiaz Lineament)
831 to the north. The Fiji plateau is located between the NFB and Lau Basin. Thin solid and dashed
832 black lines represent segments of spreading ridges/centers and fracture zones, respectively.
833 Abbreviations: Hazel Holmes Ridge (HHR), South Pandora Ridge (SPR), Tripartite Ridge (TR),
834 North Cikobia Spreading Center (NCSC), Futuna Spreading Center (FSC), North Fiji Fracture
835 Zone (NFFZ), and Central Spreading Ridge (CSR). (b) White symbols showing the sampling
836 locations on the CSR: N160 (□), N15 (○), NS (◇), 174E (▽), and Fiji Triple Junction at 16°50'S
837 (△). (c) Locations of samples from the CSR and reference sites; light brown shading shows the
838 spatial distribution of subducted slabs beneath the study area (after Richards et al., 2011). The
839 A–A' line indicates the cross-section in Fig. 12.

840 **Figure 2.** Plots of (a) total alkalis versus SiO_2 and (b–i) major elements versus MgO for the CSR
841 basalt glasses. The variations in major elements define fractional crystallization trends of two
842 different parental magma compositions, which are liquid lines of descent (LLD) for
843 DGFB120901 (solid line) and DGFB121403 (dotted line) under anhydrous (0.06 wt.% H_2O) and
844 hydrous (1 wt.% H_2O) conditions, respectively. The LLD were calculated using Petrolog3
845 (Danyushevsky & Plechov, 2011), and the Petrolog conditions were taken from Lytle et al.
846 (2012). Samples are divided into two groups with $(La/Sm)_N < 2$ (open symbols) and $(La/Sm)_N \geq$
847 2 (red symbols), which broadly correspond to the LLD for DGFB120901 and DGFB121403,
848 respectively.

849 **Figure 3.** (a) Primitive-mantle-normalized (McDonough & Sun, 1995) incompatible element
850 trace patterns and (b) chondrite-normalized (McDonough & Sun, 1995) rare earth element
851 patterns for the CSR basalts (left large panels) and adjacent regions (right small panels), South
852 Pandora Ridge (SPR; Aggrey et al., 1988; A. Price et al., 2014), Fiji ocean island basalt (OIB)-
853 and island arc tholeiitic (IAT)-type (A. Price et al., 2017; Todd et al., 2012; Wharton et al., 1994)
854 and North Fiji Fracture Zone (NFFZ; Aggrey et al., 1988; Johnson & Sinton, 1990; A. Price et al.,
855 2014, 2017). Symbols for the CSR basalts are the same as in Fig. 2.

856 **Figure 4.** Plots of (a) H_2O and (b) CO_2 contents at sample depths for the CSR basaltic glasses,
857 showing saturation curves for H_2O and CO_2 in basaltic melts (Dixon & Stolper, 1995). (c) H_2O–
858 CO_2 contents of the CSR basalts plotted with reference data for MORBs (Dixon & Stolper, 1995),
859 Mariana BABB (Newman et al., 2000), and Samoan OIBs (Workman et al., 2006). (d) Plot of
860 sampling depth versus calculated vapour-saturated depth. Symbols for the CSR basalts are the
861 same as in Fig. 2.

862 **Figure 5.** Plots of (a) $^{143}Nd/^{144}Nd$ versus $^{87}Sr/^{86}Sr$, (b) $^{87}Sr/^{86}Sr$ versus $^{206}Pb/^{204}Pb$, (c)
863 $^{143}Nd/^{144}Nd$ versus $^{206}Pb/^{204}Pb$, and (d) $^{208}Pb/^{204}Pb$ versus $^{206}Pb/^{204}Pb$, and (e) $^{207}Pb/^{204}Pb$ versus
864 $^{206}Pb/^{204}Pb$ for the CSR basalts and volcanic rocks from adjacent sites: Fiji plateau (Fiji OIBs;
865 Pearce et al., 2007; A. Price et al., 2017), South Pandora Ridge (SPR; Aggrey et al., 1988; A.
866 Price et al., 2014), Wallis (A. Price et al., 2014), Alexa Bank (Hart et al., 2004), Rotuma (A.
867 Price et al., 2017), Manatu (A. Price et al., 2014), Rochambeau Rift (RR; Lupton et al., 2009,

868 2012; Lytle et al., 2012), Futuna Spreading Center (FSC; A. Price et al., 2017), Tripartite Ridge
869 (TR; Johnson & Sinton, 1990; A. Price et al., 2017; A. Price et al., 2014), Futuna (A. Price et al.,
870 2014), Northeast Peggy Ridge (NE PR; A. Price et al., 2014), Northwest Lau Spreading Center
871 (NWLSC; Lupton et al., 2009, Lytle et al., 2012), North Fiji Fracture Zone (NFFZ; Aggrey et al.,
872 1988; Johnson & Sinton, 1990; A. Price et al., 2014, 2017). Previously reported data from the
873 CSR are also plotted (Eissen et al., 1991, 1994; Nohara et al., 1994; A. Price et al., 2014, 2017; R.
874 Price et al., 1990; R. Price & Kroenke, 1991). The reference data were compiled from GEOROC
875 (http://georoc.mpch-mainz.gwdg.de/georoc) and PetDB (http://www.earthchem.org/petdb).
876 Radiogenic isotope data for shield-stage and rejuvenated Samoan volcanic rocks (Jackson et al.,
877 2014; Konter & Jackson, 2012) are shown as grey and cyan fields in (a–d), respectively. Thick
878 dashed line in (a) is possible mixing trends between hypothetical mantle source of the Lau back-
879 arc basin basalt and EM2 component in Samoa (Nebel & Arculus, 2015). Thick solid line in (d)
880 is the Northern Hemisphere Reference Line (NHRL; Hart, 1984). Small arrows indicate trends
881 toward each mantle end-member: enriched mantle 1 (EM1) and 2 (EM2), common hotspot
882 component ("FOZO"), and depleted MORB mantle (DMM; Farley et al., 1992). Blue lines
883 indicate present-day isotopic composition of recycled oceanic crust (basalt + sediment) presented
884 with a proportion of sediment (calculated by Kimura et al., 2016).

885 **Figure 6.** Plots of ^{3}He/^{4}He versus (a) ^{4}He content, (b) ^{87}Sr/^{86}Sr, (c) ^{143}Nd/^{144}Nd, and (d)
886 ^{206}Pb/^{204}Pb for the CSR basalts and volcanic rocks from adjacent regions. Symbols are the same
887 as in Fig. 1c. Isotopic compositions for Iceland, Loihi, and depleted MORB mantle (DMM) are
888 shown, along with those of sediment (Sed), altered oceanic crust (AOC), and HIMU (Zindler &
889 Hart, 1986).

890 **Figure 7.** Latitudinal variation of (a) sampling depth and (b–h) geochemical data along the CSR.
891 Symbols for the CSR basalts are the same as in Fig. 2. (a, e–h) OIB-like enriched features of
892 high $(La/Sm)_N$, radiogenic Sr–Pb, and less radiogenic Nd are observed in the northern CSR
893 segments, whereas relatively depleted MORB-like compositions (both N- and E-MORBs) are
894 found in all of the segments. (c–d) Variations of $Na_{8.0}$ and H_2O indicate that the degree of
895 melting along the CSR is associated with decompression melting beneath the mid-ocean ridges
896 rather than flux-controlled melting controlled by the water content in the sub-arc mantle. (e–h)
897 ^{3}He/^{4}He ratios show distinctive variations with latitude suggesting that some process decouples
898 the He and Sr–Nd–Pb isotopes.

899 **Figure 8.** Diagrams used to identify the tectonic setting and melting conditions of the CSR
900 basalts. Symbols are the same as in Fig. 1c. (a) La/Sm versus Ba/Nb. CSR basalts exhibit a trend
901 between depleted and enriched mantle. An insignificant increase in Ba/Nb with La/Sm indicates
902 subduction effects were negligible in the northern CSR. (b) Ti/Y versus Nb/Y (after Pearce,
903 1982). Data for the CSR basalts are plotted with the fields for mid-ocean ridge and within-plate
904 basalts. The enriched CSR basalts plot in the field of within-plate basalts. (c) Yb versus La/Yb
905 after Baker et al. (1997) and (d) La/Sm versus Sm/Yb after Özdemir & Güleç, (2014) with
906 calculated partial melting curves for spinel (Sp) and garnet (Gt) lherzolites. The CSR basalts
907 contain variable proportions of melt from garnet and spinel lherzolite.

908 **Figure 9.** EM1-type features of the enriched CSR basalts shown on plots of (a) Ba/Th versus
909 Zr/Hf after Konter & Jackson (2012), (b) Ba/Th versus Zr/Th modified after Reinhard et al.
910 (2019), and (c) Ba/Ta versus La/Ta modified from Gorring et al. (2003). Symbols are the same

as in Fig. 1c. (a) Data for the CSR basalts plotted with the fields for MORBs (East Pacific Rise) and EM1 (Rarotonga; Konter & Jackson, 2012). The MORB-like CSR basalts exhibit a positive correlation between Ba/Th and Zr/Hf, whereas the OIB-like CSR basalts plot in the field of EM1 (Rarotonga and rejuvenated Samoa) and have a negative correlation. (b) The OIB-like CSR basalts show a strong affinity with rejuvenated Samoan volcanic rocks (EM1) relative to shield-stage Samoan volcanic rocks (i.e., the Malu trend of EM2, Vai trend of HIMU, and Upo trend of DM; Jackson et al., 2014; Reinhard et al., 2019). (c) The OIB-like CSR basalts and some MORB-like samples with high Ba/La ratios (> 10) plot in the field of rejuvenated Samoan volcanic rocks (Konter & Jackson, 2012; Reinhard et al., 2019).

Figure 10. Diagram of the principal component analysis (PCA) of geochemical proxies used in Fig. 5, 6 and 9 (Sr-Nd-Pb-He isotopes, Ba/Th, Ba/Ta, La/Ta, Zr/Hf, and Zr/Th in right panel). Samples from the shield-stage and rejuvenated Samoa (open symbols represent data from Konter & Jackson, 2012; filled symbols represent data from Reinhard et al., 2019) and the Pitcairn (Eisele et al., 2002) are included in a source data for the PCA. The enriched CSR basalts have high Ba/Th and Ba/Ta ratios similar to the South Pandora Ridge and Wallis samples. Those high Ba-rich samples are distinct from the shield-stage Samoan lavas and close to the rejuvenated Samoa and Pitcairn of EM1 component, indicating an alternative enrichment process to the Samoan plume material. The Alexa Bank, Futuna Spreading Center and Peggy Ridge samples are not presented due to absence of some variables.

Figure 11. Plot of H_2O/Ce versus Ba/Th showing the possible mantle sources of the CSR basalts (after Chen et al., 2017). Mixing of depleted MORB mantle and dehydrated altered oceanic crust and sediments can account for the geochemical heterogeneity of the CSR basalts.

Figure 12. Schematic illustration of the upper-mantle origin of EM1-signature in the trench-distal back-arc basin. Tectonic setting and slab stagnation in the NFB are presented in A–A' cross-section of Fig. 1c, based on Faccenna et al. (2010) and Richards et al. (2011). Enriched components in the asthenosphere, which are derived by mantle upwelling above the edge of a flat-lying slab in the mantle transition zone (Yang & Faccenda, 2020), are the dominant source for the OIB-like melts in the mature back-arc basin.
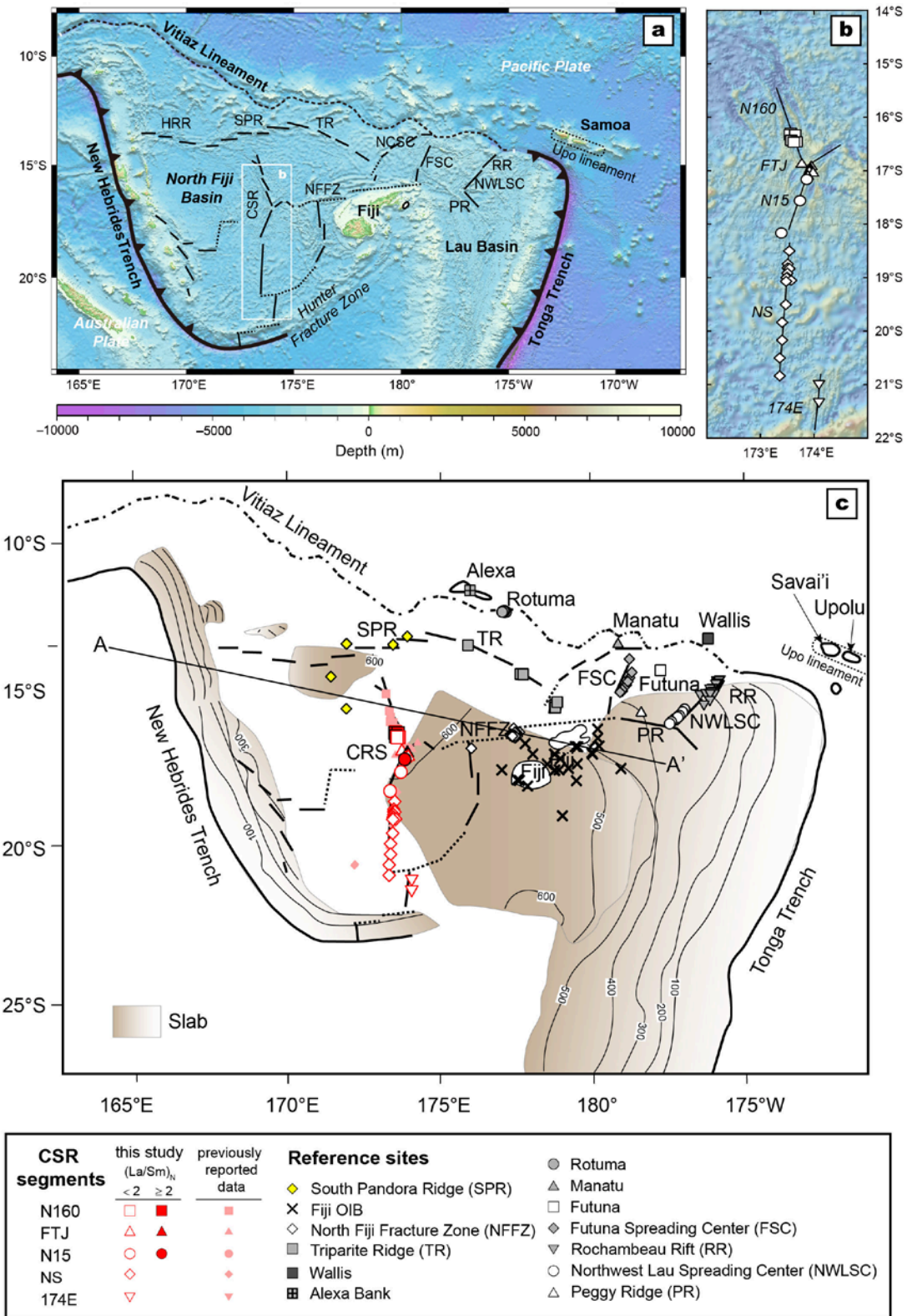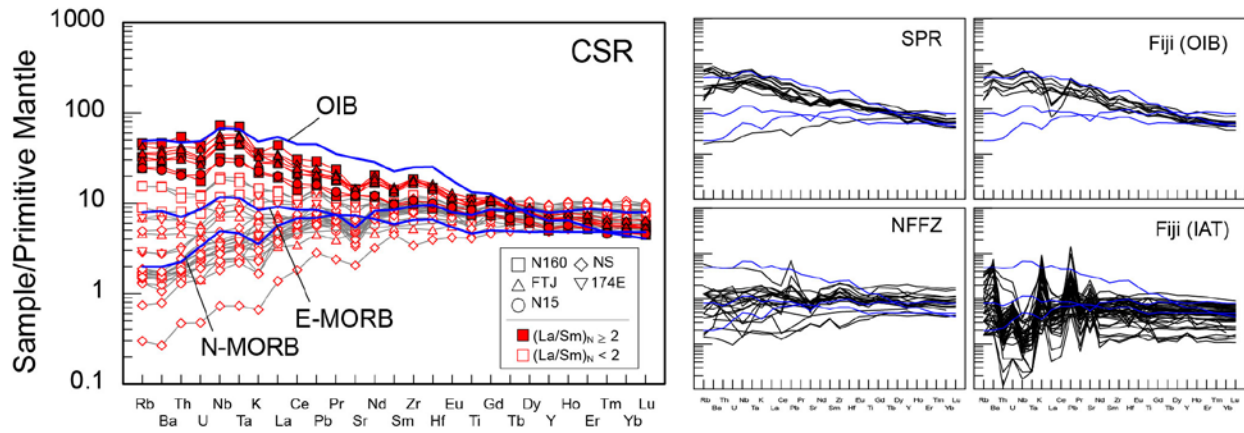
Figure 1

942
943   Figure 2
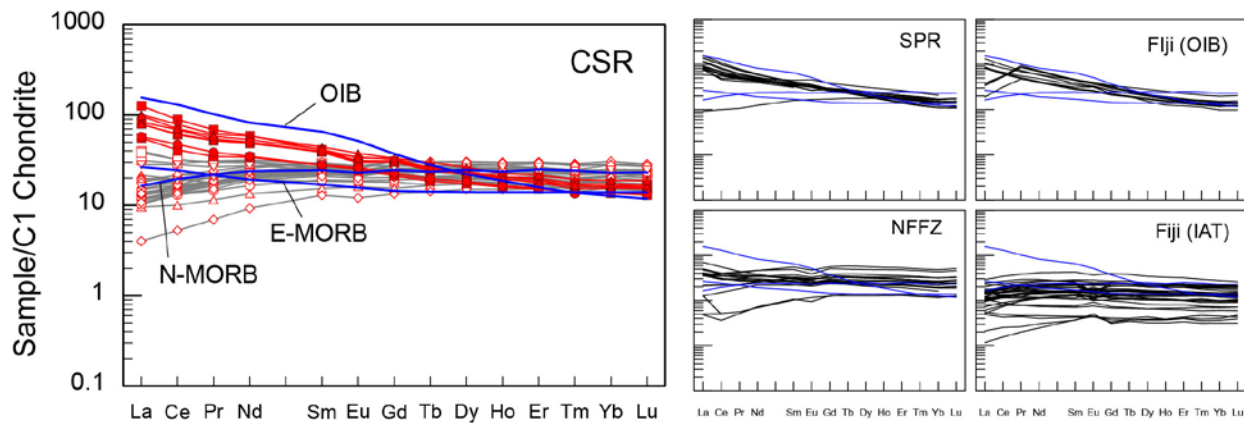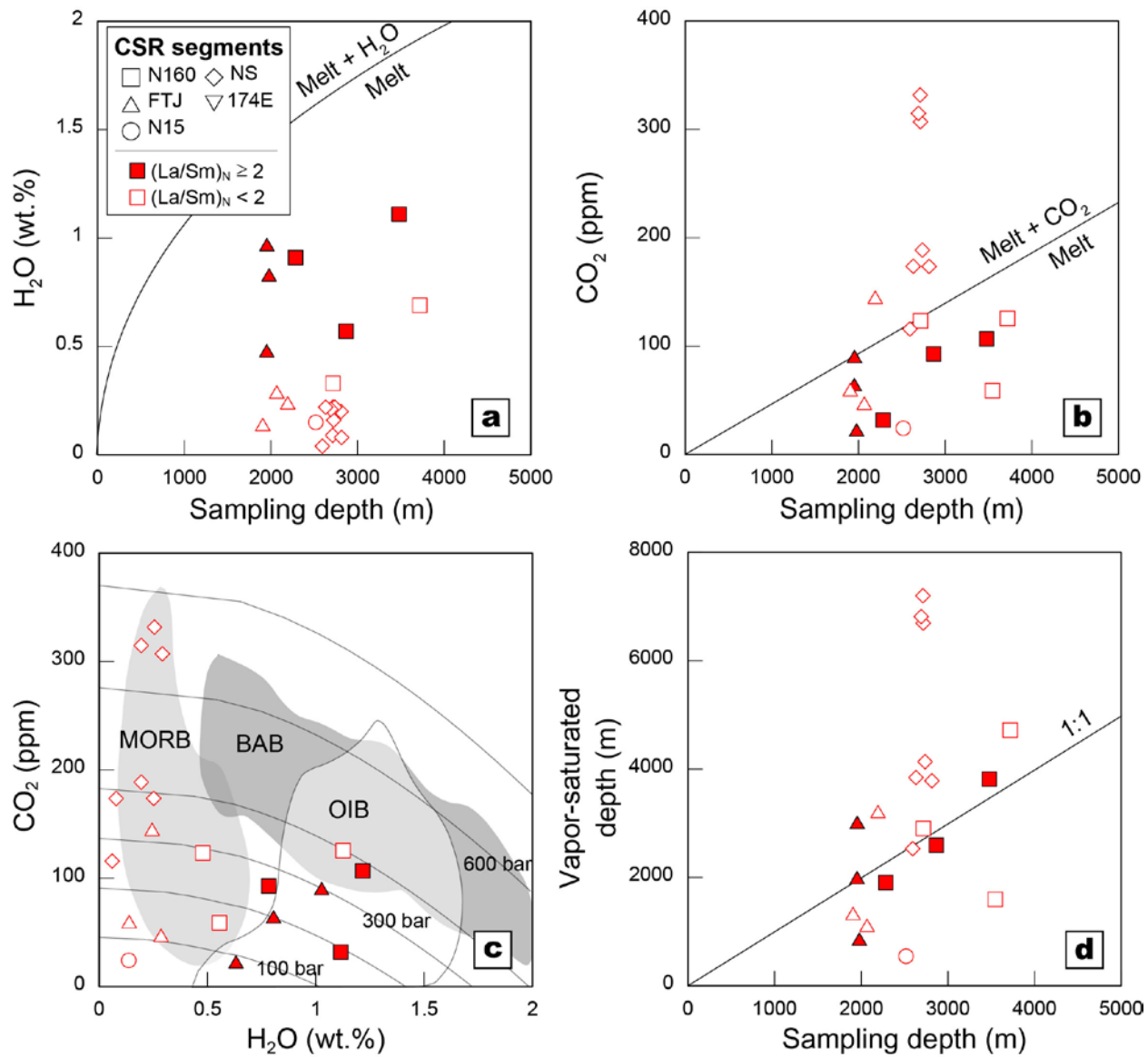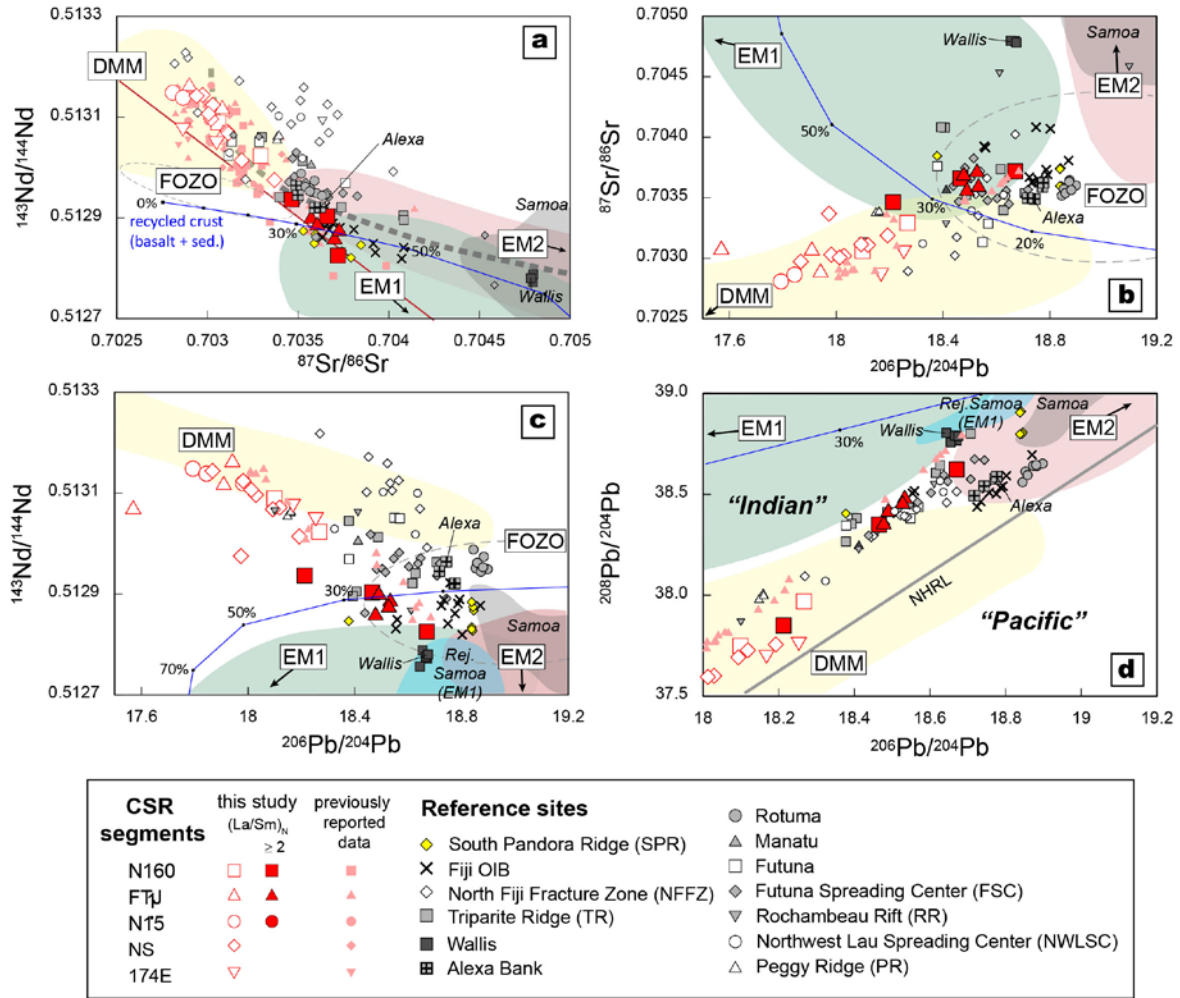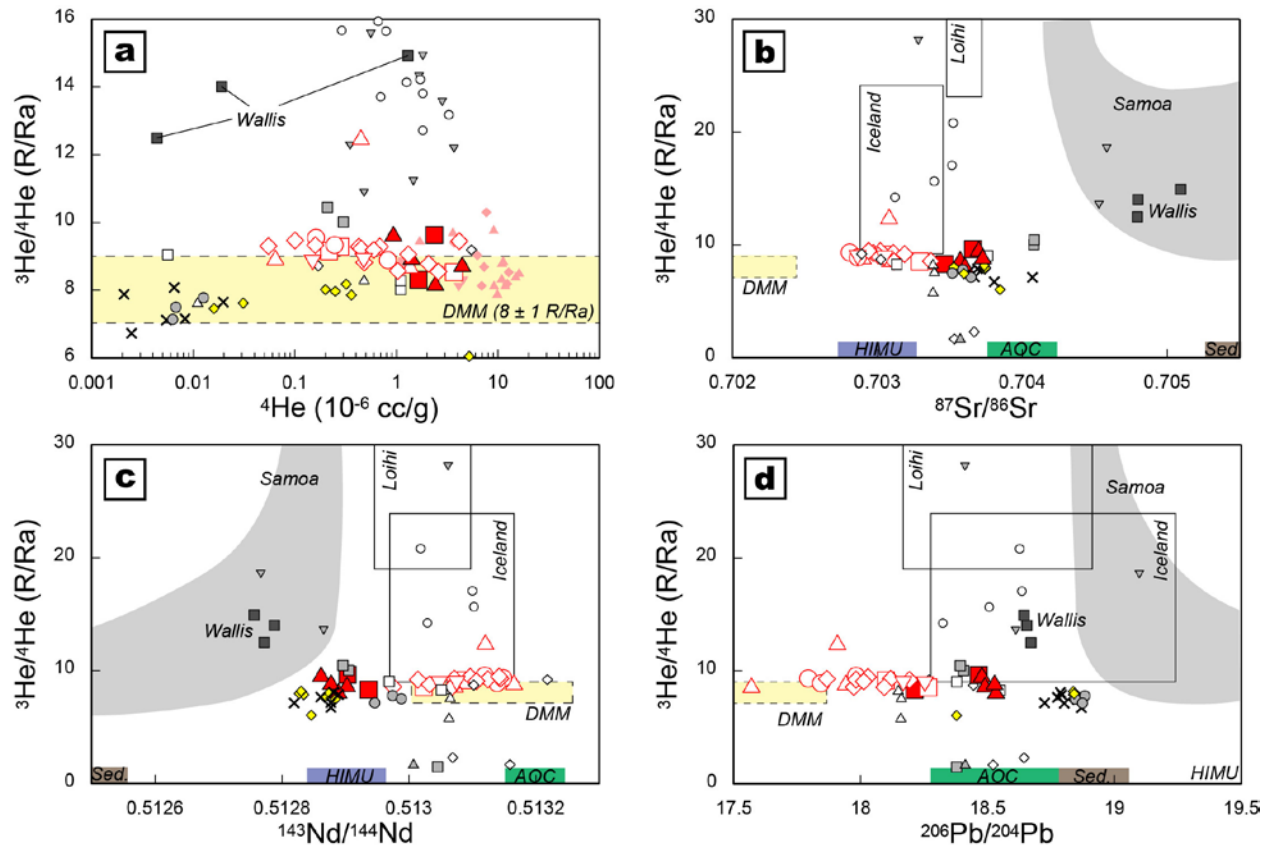
944
945
946   Figure 3
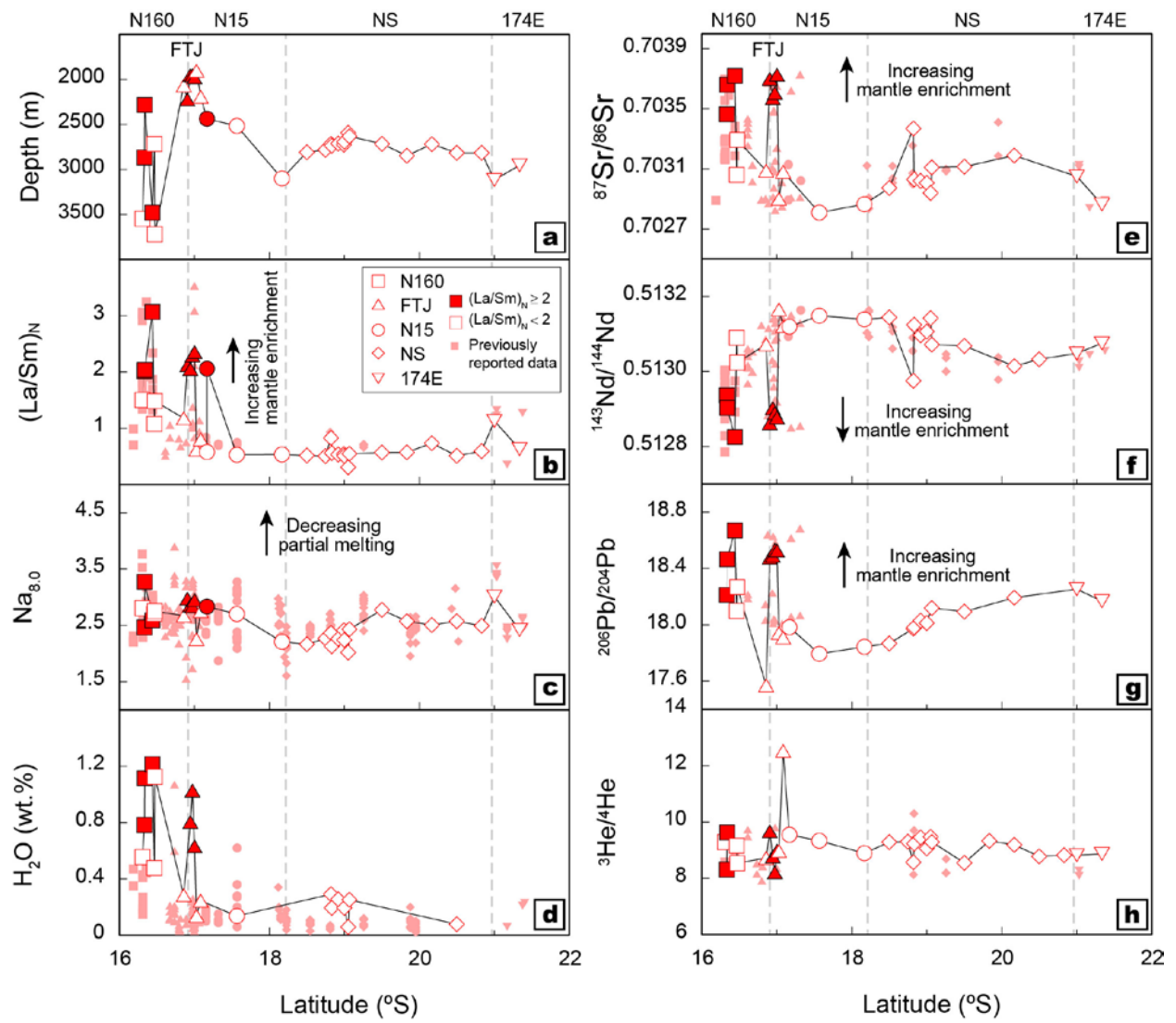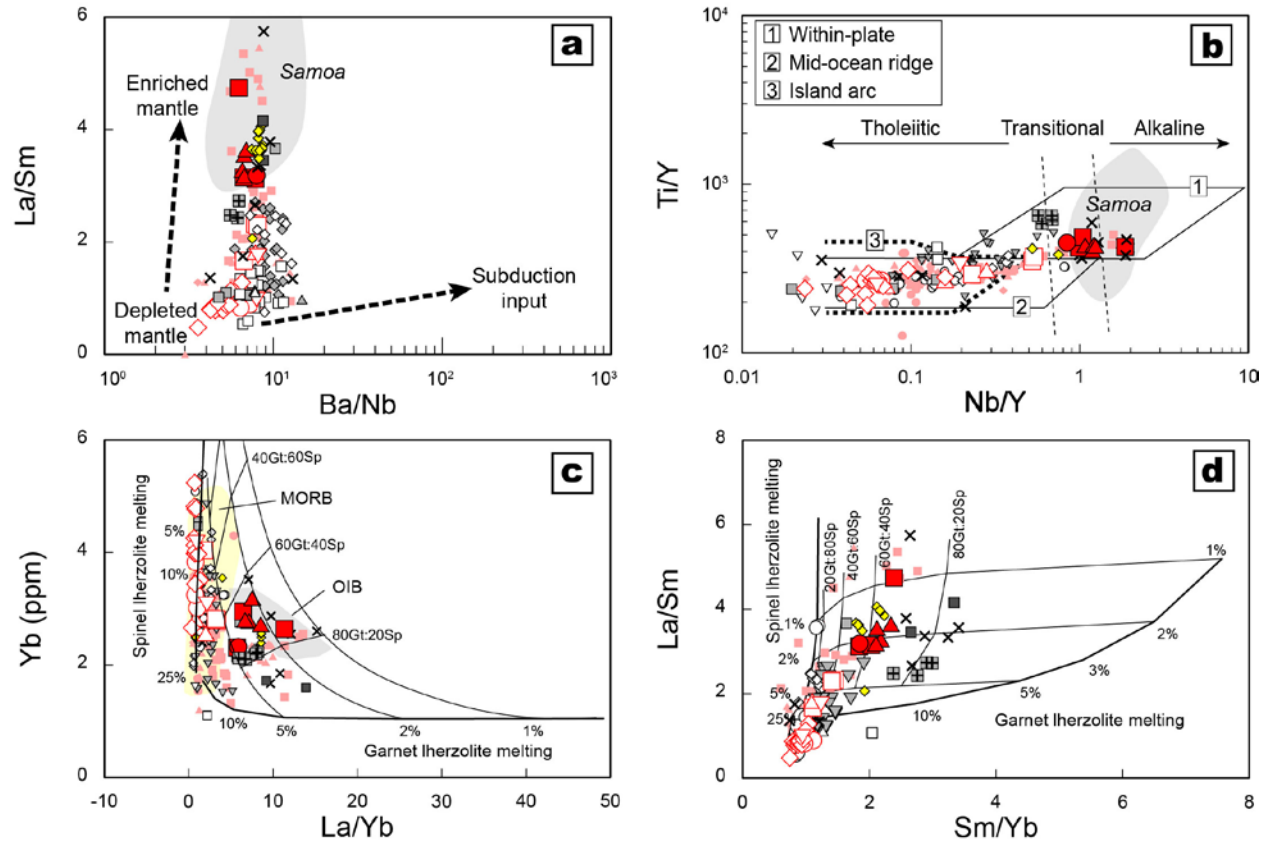947
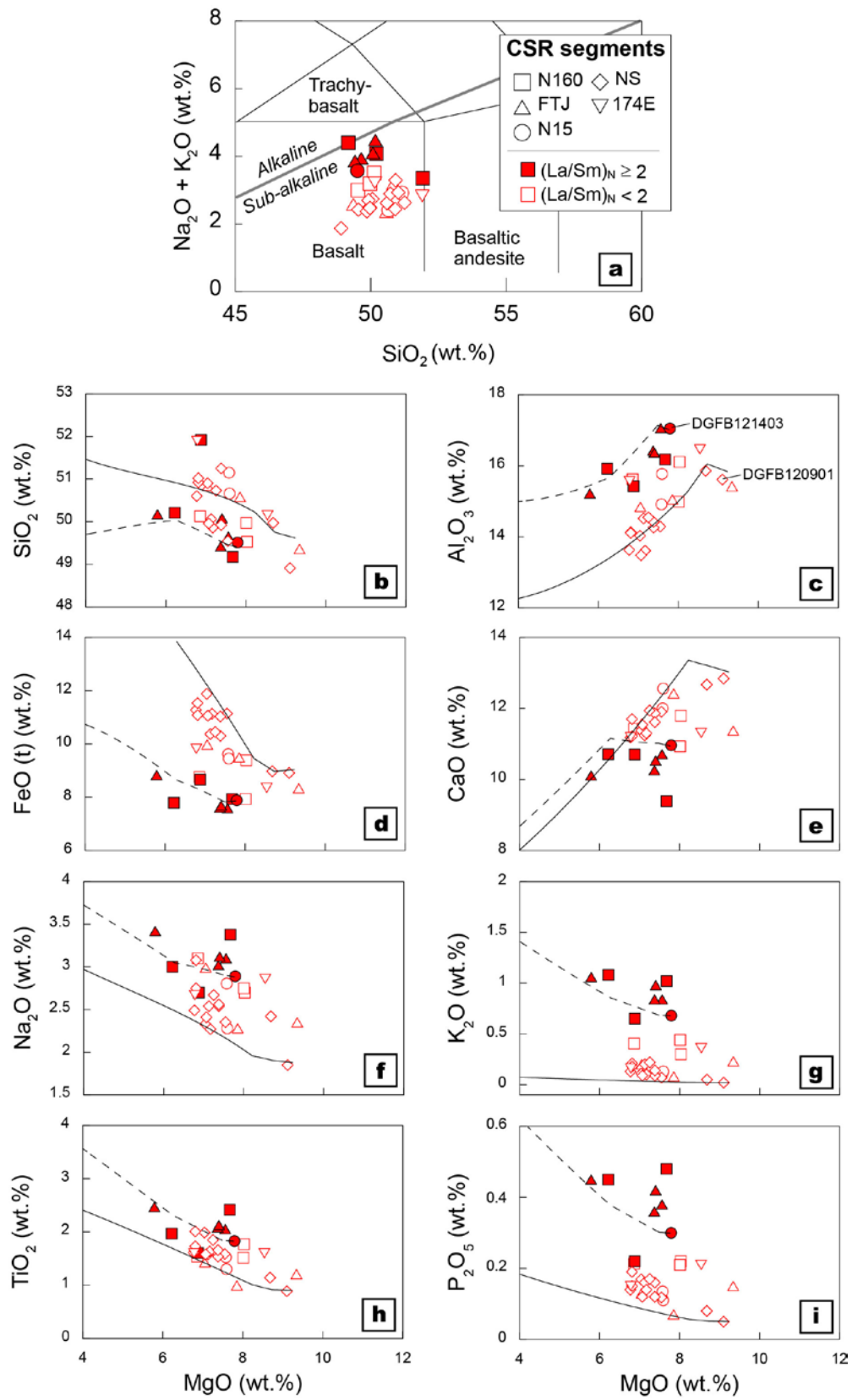
948
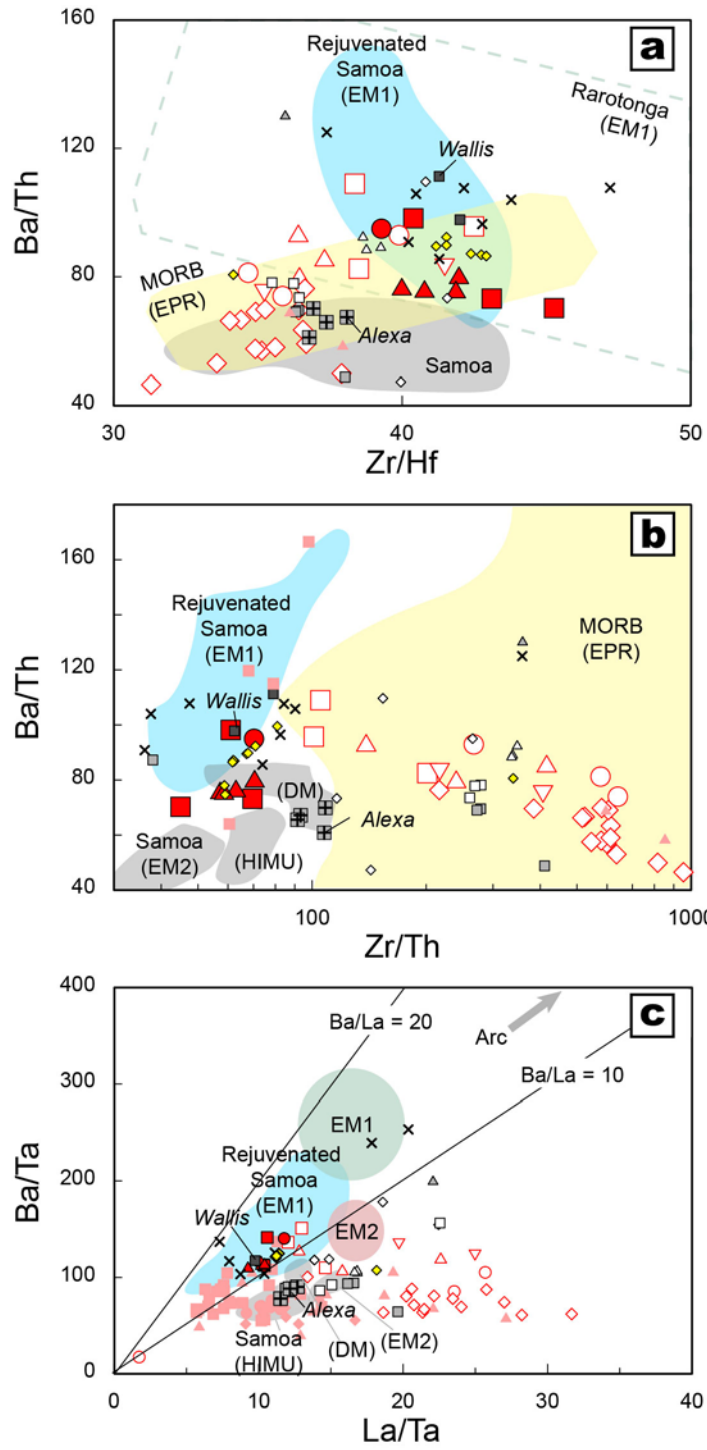949   Figure 4
950

951
952   Figure 5
953

954
955   Figure 6
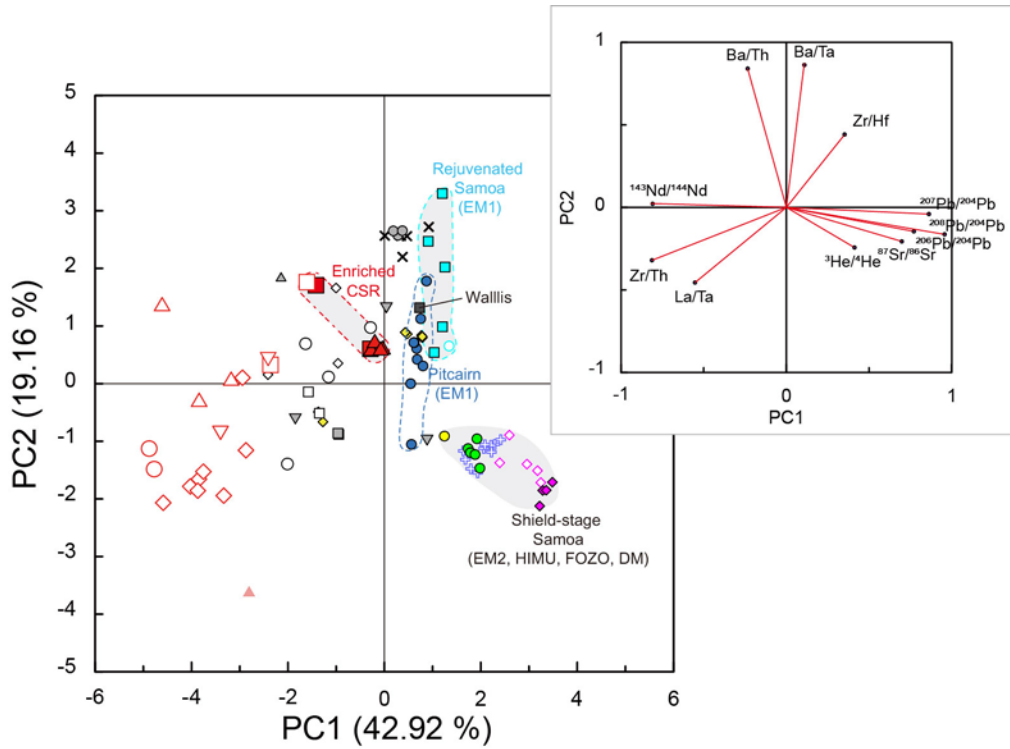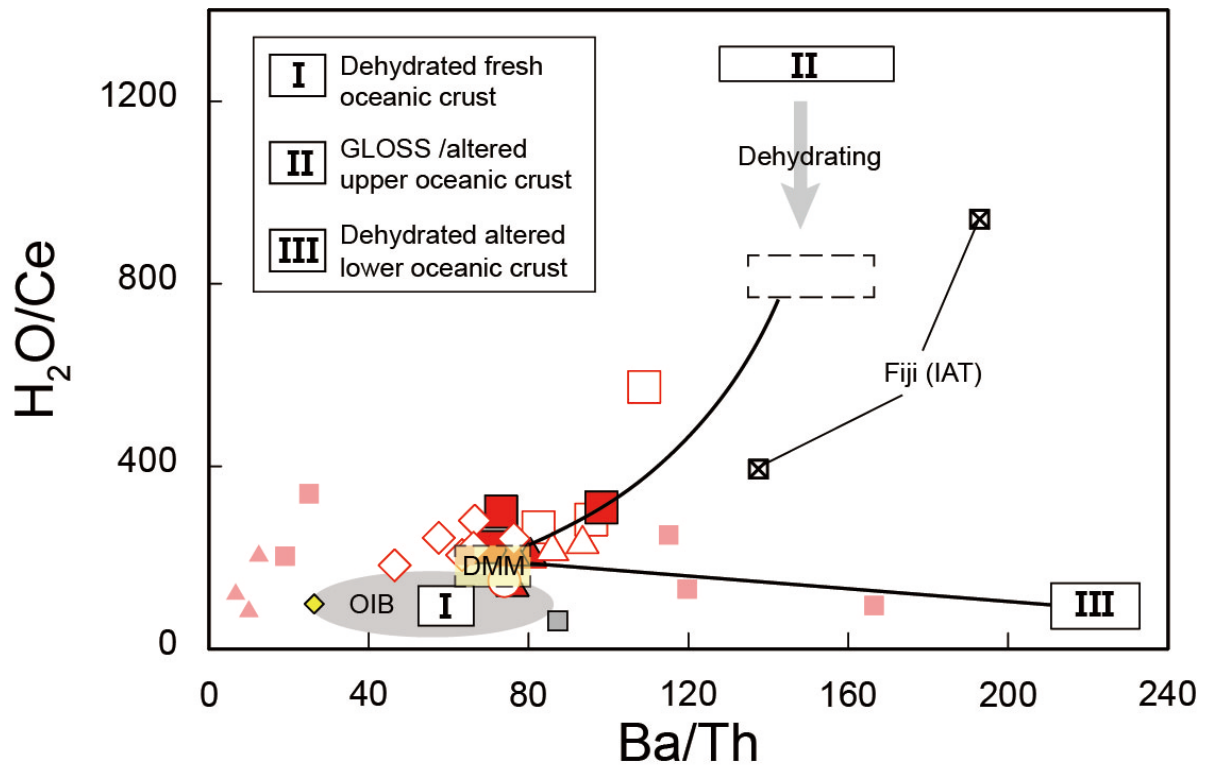
956
957
958   Figure 7

959
960
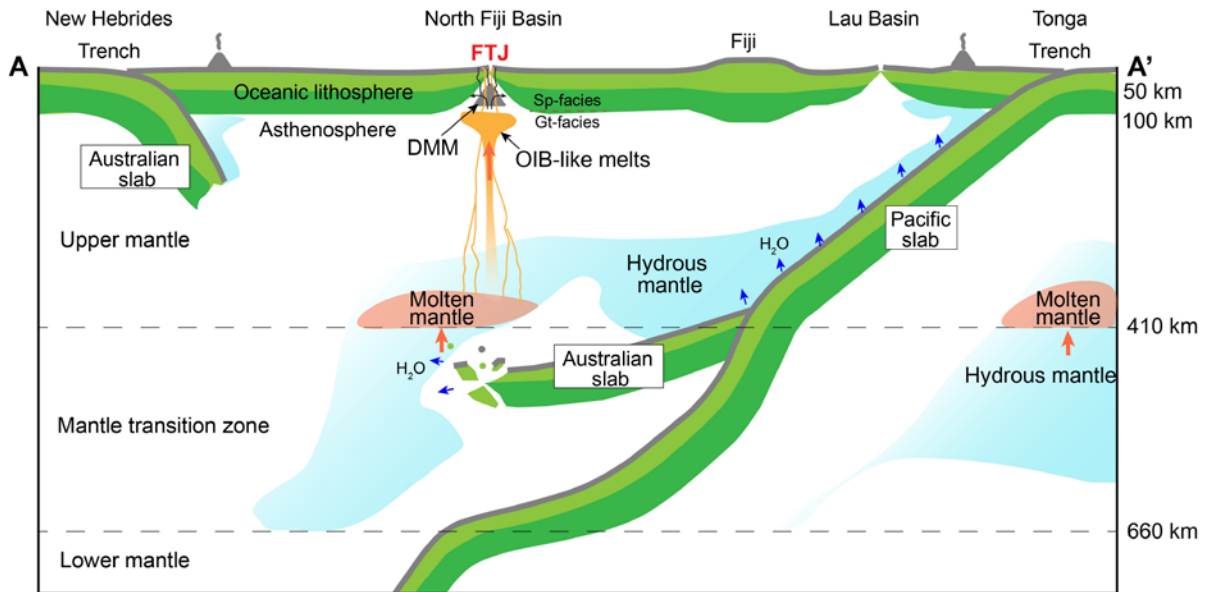961   Figure 8

962
963
964   Figure 9

965
966
967
968   Figure 10
969

970
971
972   Figure 11
973

974
975

976
977   Figure 12
978